nature aging

ARTICLES

https://doi.org/10.1038/s43587-021-00164-x

Check for updates

OPEN

Scinderin promotes fusion of electron transport chain dysfunctional muscle stem cells with myofibers

Xun Wang[1], Spencer D. Shelton[1], Bogdan Bordieanu[1,10], Anderson R. Frank[2,7], Yating Yi[3,11], Siva Sai Krishna Venigalla[1], Zhimin Gu[1], Nicholas P. Lesner[1,12], Michael Glogauer[4], Navdeep S. Chandel[5,6], Hu Zhao[3,13], Zhiyu Zhao[1], David G. McFadden[2,7,8] and Prashant Mishra[1,8,9] ✉

Muscle stem cells (MuSCs) experience age-associated declines in number and function, accompanied by mitochondrial electron transport chain (ETC) dysfunction and increased reactive oxygen species (ROS). The source of these changes, and how MuSCs respond to mitochondrial dysfunction, are unknown. We report here that in response to mitochondrial ROS, murine MuSCs directly fuse with neighboring myofibers; this phenomenon removes ETC-dysfunctional MuSCs from the stem cell compartment. MuSC–myofiber fusion is dependent on the induction of Scinderin, which promotes formation of actin-dependent protrusions required for membrane fusion. During aging, we find that the declining MuSC population accumulates mutations in the mitochondrial genome but selects against dysfunctional variants. In the absence of clearance by Scinderin, the decline in MuSC numbers during aging is repressed; however, ETC-dysfunctional MuSCs are retained and can regenerate dysfunctional myofibers. We propose a model in which ETC-dysfunctional MuSCs are removed from the stem cell compartment by fusing with differentiated tissue.

Mitochondrial ETC dysfunction impacts the human population in multiple ways. Germline mutations in the mitochondrial and nuclear genome are estimated to affect as many as 1:5,000 individuals[1], and accumulating ETC dysfunction is also observed as a secondary component of many common diseases, including aging itself[2–4]. Examining the mechanistic consequences of ETC dysfunction in various differentiated tissues has therefore been important to understanding disease physiology and progression. In contrast, our current knowledge of the consequences of ETC dysfunction in stem cell compartments has been understudied, despite the regenerative potential of these cells. In hematopoietic stem cells, depletion of complex III or mitochondrial DNA (mtDNA) results in impaired differentiation and anemia, as well as stem cell exhaustion[5,6]. However, despite numerous studies of metabolic changes in various stem cell types, a direct analysis of the consequences of ETC dysfunction is largely missing, including in MuSCs. MuSCs are largely quiescent and nonproliferative during adult life. In response to injury, quiescent MuSCs undergo rapid activation and proliferation, followed by cell fusion to regenerate new myofibers. Activated MuSCs exhibit altered metabolism to drive differentiation and have an high capacity to expand their mitochondrial population during formation of a new myofiber[7,8]. Whether there are unique mechanisms to maintain ETC functionality in MuSCs is currently unclear.

We report here that MuSCs are sensitive to ETC dysfunction associated with oxidative stress. We propose a model in which in response to elevated superoxide levels, MuSCs undergo a unique fate to be rapidly removed from muscular tissue, which is mediated by direct fusion of quiescent stem cells with preexisting myofibers. In this manner, ETC-dysfunctional MuSCs are deleted from the stem cell population and are thereby precluded from regenerating dysfunctional tissue. We identify that the MuSC–myofiber fusion event is downstream of ROS generation and dependent on the induced expression of an actin-network reorganizing protein, Scinderin. In the absence of Scinderin-mediated fusion, ETC-dysfunctional MuSCs remain and are competent to regenerate dysfunctional tissue. Thus, MuSCs retain a unique mechanism governing their response to ETC deficiency.

Results

Complex IV inhibition depletes MuSCs by MuSC–myofiber fusion. We examined the consequences of ETC dysfunction using genetic models in which complex IV activity was conditionally depleted in adult murine MuSCs. Using the *Pax7-Cre*$^{ERT2(FAN)}$ driver (which induces tamoxifen-dependent recombination in satellite cells, a subset of MuSCs critical for muscle regeneration[9–11]) and a floxed *Cox10* (an accessory subunit of mitochondrial complex IV)

[1]Children's Medical Center Research Institute, University of Texas Southwestern Medical Center, Dallas, TX, USA. [2]Department of Biochemistry, University of Texas Southwestern Medical Center, Dallas, TX, USA. [3]Department of Comprehensive Dentistry, College of Dentistry, Texas A&M University, Dallas, TX, USA. [4]Faculty of Dentistry, University of Toronto, Toronto, Ontario, Canada. [5]Department of Medicine, Northwestern University Feinberg School of Medicine, Chicago, IL, USA. [6]Department of Biochemistry & Molecular Genetics, Northwestern University Feinberg School of Medicine, Chicago, IL, USA. [7]Department of Internal Medicine, Division of Endocrinology, Program in Molecular Medicine, University of Texas Southwestern Medical Center, Dallas, TX, USA. [8]Harold C. Simmons Comprehensive Cancer Center, University of Texas Southwestern Medical Center, Dallas, TX, USA. [9]Department of Pediatrics, University of Texas Southwestern Medical Center, Dallas, TX, USA. [10]Present address: Department of Neuroscience, Medical University of South Carolina, Charleston, SC, USA. [11]Present address: State Key Laboratory of Oral Diseases, National Clinical Research Center for Oral Diseases, Department of Orthodontics, West China Hospital of Stomatology, Sichuan University, Chengdu, Sichuan, China. [12]Present address: Abramson Family Cancer Research Institute, Perelman School of Medicine, University of Pennsylvania, Philadelphia, PA, USA. [13]Present address: The Chinese Institute for Brain Research, Beijing, China. ✉e-mail: prashant.mishra@utsouthwestern.edu

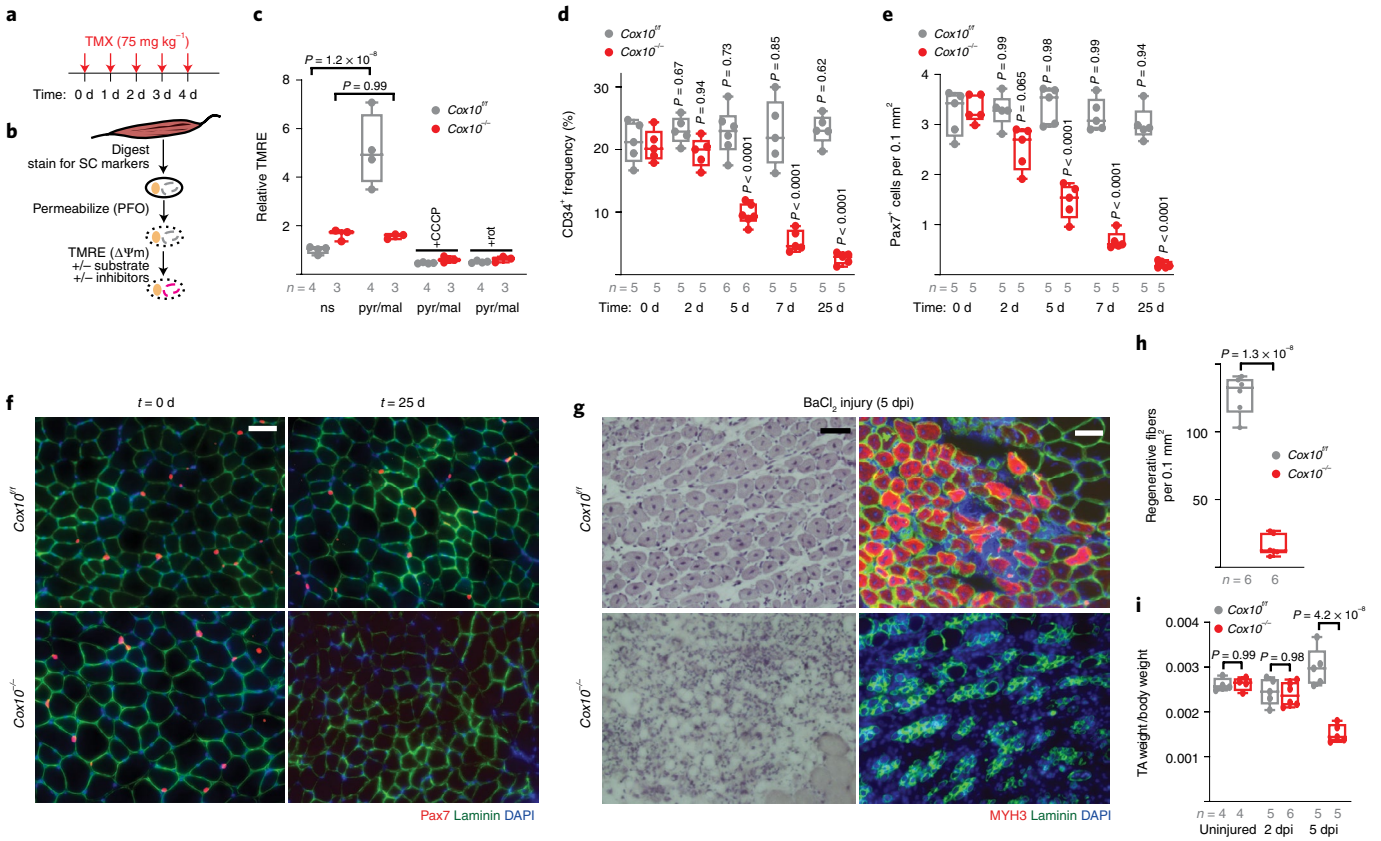

Fig. 1 | Complex IV dysfunction induces rapid MuSC depletion in vivo. a, Schematic for the tamoxifen (TMX) administration protocol to induce recombination in adult MuSCs. **b**, FACS-based assay for ETC function. Isolated MuSCs are permeabilized with perfringolysin O (PFO), followed by TMRE staining in the presence or absence of mitochondrial substrates and inhibitors. SC, stem cell. **c**, Mean TMRE fluorescence of wild-type (*Cox10*$^{f/f}$) and *Cox10*$^{-/-}$ MuSCs in response to indicated substrates and inhibitors. ns, no substrate; pyr/mal, pyruvate/malate; rot, rotenone. **d**, MuSC frequency at indicated time points after the first dose of tamoxifen in mice with *Cox10*$^{f/f}$ or *Cox10*$^{-/-}$ MuSCs. *P* values reflect comparisons with $t = 0$ day data for each genotype. **e**, Pax7^{+} cell numbers (normalized to muscle area) at different times after the first dose of tamoxifen. *P* values reflect comparisons with $t = 0$ day data for each genotype. **f**, Representative images of endogenous Pax7^{+} cells (red), Laminin (green) and DAPI (blue) from tibialis anterior (TA) cross sections of indicated mice at different times after tamoxifen administration. Scale bar, 50 µm. **g**, Histology (H&E staining) and immunofluorescence images of TA cross sections 5 days after barium chloride ($BaCl_2$) injury. Regenerative myofibers can be identified by their centrally localized nuclei and MYH3-positive staining at this timepoint. Scale bars, 50 µm. **h**, Quantitation of regenerative (central nuclei) myofibers (normalized to muscle area) in TA muscles 5 days after $BaCl_2$ injury. **i**, TA weight (normalized to body weight) at various time points after $BaCl_2$ injury. Statistical significance was assessed using two-way analysis of variance (ANOVA) (**c**–**e**,**i**) or two-tailed *t* test (**h**) with adjustments for multiple comparisons. Box plots indicate median values and interquartile ranges; whiskers are plotted using the Tukey method. The number of biological replicates in each group and *P* values are indicated in the figure. Experiments were repeated five times (**f**) and six times (**g**), with similar results. d, days; DAPI, 4,6-diamidino-2-phenylindole; dpi, days postinjury.

allele (*Cox10*^{f})[12,13], we depleted *Cox10* transcript and protein levels in adult MuSCs using a 5-day tamoxifen administration (Fig. 1a and Extended Data Fig. 1a). To assess whether ETC function was impaired in our experimental model, we implemented an in vitro fluorescence-activated cell sorting (FACS)–based assay amenable to rare cell populations (Fig. 1b). Acutely isolated MuSCs were permeabilized and incubated with or without mitochondrial substrates in the presence of TMRE (tetramethylrhodamine ethyl ester; whose fluorescence is a measure of mitochondrial membrane potential ($\Delta\Psi_m$)). In MuSCs from tamoxifen-treated control mice (*Cox10*$^{f/f}$; no Pax7-Cre driver; hereafter *Cox10*$^{f/f}$), mitochondrial substrates stimulated TMRE fluorescence, which was blocked by ETC inhibitors (e.g., rotenone) or uncouplers (carbonyl cyanide 3-chlorophenylhydrazone (CCCP)), indicating the presence of a functional ETC (Fig. 1c and Extended Data Fig. 1b). In contrast, *Cox10*$^{-/-}$ MuSCs (from tamoxifen-treated *Pax7-Cre*$^{ERT2(FAN)}$; *Cox10*$^{f/f}$ mice; hereafter *Cox10*$^{-/-}$) exhibited impaired stimulation of mitochondrial membrane potential, indicating significant ETC dysfunction in this stem cell compartment (Fig. 1c and Extended Data Fig. 1b). In addition, *Cox10*$^{-/-}$ MuSCs exhibited significant increases in mitochondrial mass, consistent with ETC dysfunction (Extended Data Fig. 1c).

Deletion of *Cox10* by tamoxifen administration induced a progressive decrease in MuSC numbers, as assed by the frequency of CD34^{+}CD31^{-}CD45^{-}Sca1^{-} cells by flow cytometry or staining of endogenous Pax7 in tissue sections (Fig. 1d–f and Extended Data Fig. 1d). As expected, the dramatic loss of MuSCs was associated with a severe regeneration defect in response to muscle cryoinjury (Extended Data Fig. 1e–h) or chemically induced muscular injury (Fig. 1g–i), as evidenced by a lack of activated (myogenin-positive (Myog^{+})) MuSCs and regenerative (myosin heavy chain 3–positive (MYH3^{+})) myofibers and impaired recovery of muscle mass. These results were confirmed using a second independent *Pax7-Cre*$^{ERT2(KARDON)}$ allele[11], which also resulted in the loss of Pax7^{+} MuSCs cells upon tamoxifen-induced deletion of *Cox10* (Extended Data Fig. 1i,j), accompanied by regenerative defects in response to injury (Extended Data Fig. 1k,l).

Cellular stress in MuSCs has been previously associated with premature activation or differentiation;[14] however, we did not observe

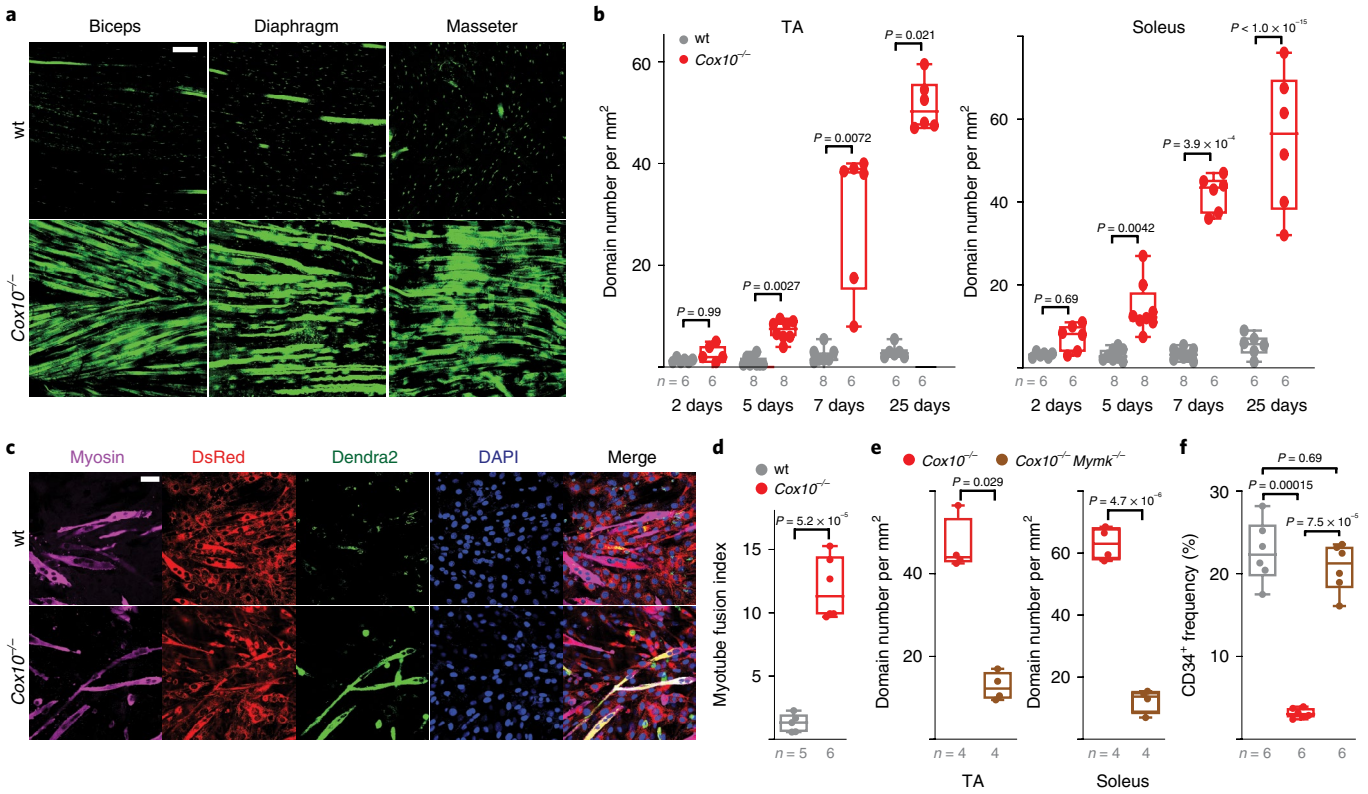

Fig. 2 | Complex IV dysfunction induces MuSC–myofiber fusion in vivo and in vitro. a, Longitudinal imaging of mito-Dendra2 signal in various muscles 21 days after the first dose of tamoxifen. Scale bar, 200 µm. **b**, Mito-Dendra2 domain number (normalized to muscle area) in myofibers of TA and soleus muscles at different times after the first dose of tamoxifen. **c**, In vitro MuSC–myotube fusion assay. Dendra2$^+$ (green) freshly isolated MuSCs of the indicated genotype were overlaid on DsRed$^+$ (red) C2C12 myotubes and assessed for fusion with myosin-positive (magenta) myotubes after 4 days. Cells were stained with myosin (magenta) and DAPI (blue). Scale bar, 50 µm. **d**, Quantitated myotube fusion indices for MuSCs of the indicated genotype. **e**, mito-Dendra2 domain numbers in TA and soleus muscles 21 days after the first dose of tamoxifen in mice of the indicated genotype. *Mymk*, *Myomaker*. **f**, MuSC (CD34$^+$) frequency of the indicated genotypes 21 days after the first dose of tamoxifen (same color scheme as **d**,**e**). Statistical significance was assessed using two-way ANOVA (**b**), two-tailed *t* test (**d**,**e**), Kruskal–Wallis (**b**), two-tailed Mann–Whitney (**e**) or one-way ANOVA (**f**) tests with adjustments for multiple comparisons. Box plots indicate median values and interquartile ranges; whiskers are plotted using the Tukey method. The number of biological replicates in each group and *P* values are indicated in the figure. Experiments were repeated three times (**a**) and five or six times (**c**), with similar results.

indicators of myogenic activation in *Cox10*$^{-/-}$ MuSCs (Extended Data Fig. 1m). To more directly assess the fate of *Cox10*-deleted MuSCs, we attempted to synchronize Cre-mediated recombination with a single high dose of tamoxifen[15], which was sufficient to rapidly induce near-complete recombination, as well as loss of Cox10 protein (Extended Data Fig. 2a–d). This alternate protocol increased the kinetics of MuSC depletion, as detected by the CD34$^+$ population (via FACS) or the Pax7$^+$ population (via immunodetection of endogenous Pax7) (Extended Data Fig. 2e–g). Assessment of tissues at different time points after tamoxifen treatment revealed that the rapid depletion of MuSCs in this protocol was not associated with stem cell activation, apoptosis or senescence, as revealed by examination of myogenic regulatory factors (myogenic differentiation 1 (Myod), Myog and MYH3), TUNEL or β-galactosidase staining (Extended Data Figs. 3a–d and 4a–c). Although mitochondrial ETC impairment can be associated with apoptotic cell death in vitro[16,17], Cox10 deficiency has not been typically associated with acute cell death in vivo[13,18–21], and correspondingly, we did not observe any indication of apoptosis in *Cox10*$^{-/-}$ MuSCs based on TUNEL staining and assessment of cleaved caspase-3 levels (Extended Data Fig. 4d,e).

To directly determine the fate of *Cox10*$^{-/-}$ MuSCs, we performed lineage tracing using a conditional (Cre-dependent) mito-Dendra2 expression allele (*D*^{f})[22], which encodes a fluorescent protein (Dendra2) targeted to mitochondria. In control mice (*Pax7-Cre*$^{ERT2(KARDON)}$; *D*$^{f/f}$; *Cox10*$^{+/+}$; hereafter "wt"), the mito-Dendra2 signal mainly labeled mononuclear cells throughout skeletal muscle tissue (Fig. 2a), with occasional labeling of mitochondria within myofibers. Since MuSCs are known to occasionally fuse with neighboring myofibers in wild-type animals[23–25], these MuSC–myofiber fusion events can be marked by segments or 'domains' of mito-Dendra2 signal within myofibers and typically represent fusion of a single MuSC[25]. *Cox10* deletion in MuSCs (*Cox10*$^{-/-}$: *Pax7-Cre*$^{ERT2(KARDON)}$; *D*$^{f/f}$; *Cox10*$^{f/f}$) dramatically increased the frequency of mito-Dendra2 domains within myofibers (Fig. 2a), corresponding to an elevated rate of MuSC fusion into myofibers. The contribution of MuSCs to neighboring myofibers accumulated with time after tamoxifen administration, occurred in multiple muscles throughout the body and was randomly distributed through muscle tissue, as revealed by deep imaging of cleared tissue (Fig. 2a,b and Supplementary Videos 1–3). Fiber-type analysis revealed that MuSCs readily fused to both slow- (type I) and fast-twitch (type II) fibers, with a statistical preference for slow-twitch fibers (Extended Data Fig. 5a–c). Single-fiber analysis indicated that mitochondrial content was not notably increased in myofiber segments where a fusion event had occurred (Extended Data Fig. 5d–f).

Quantitating the number of spatially distinct domains (Fig. 2b), or the number of fibers receiving a labeled MuSC (Extended Data

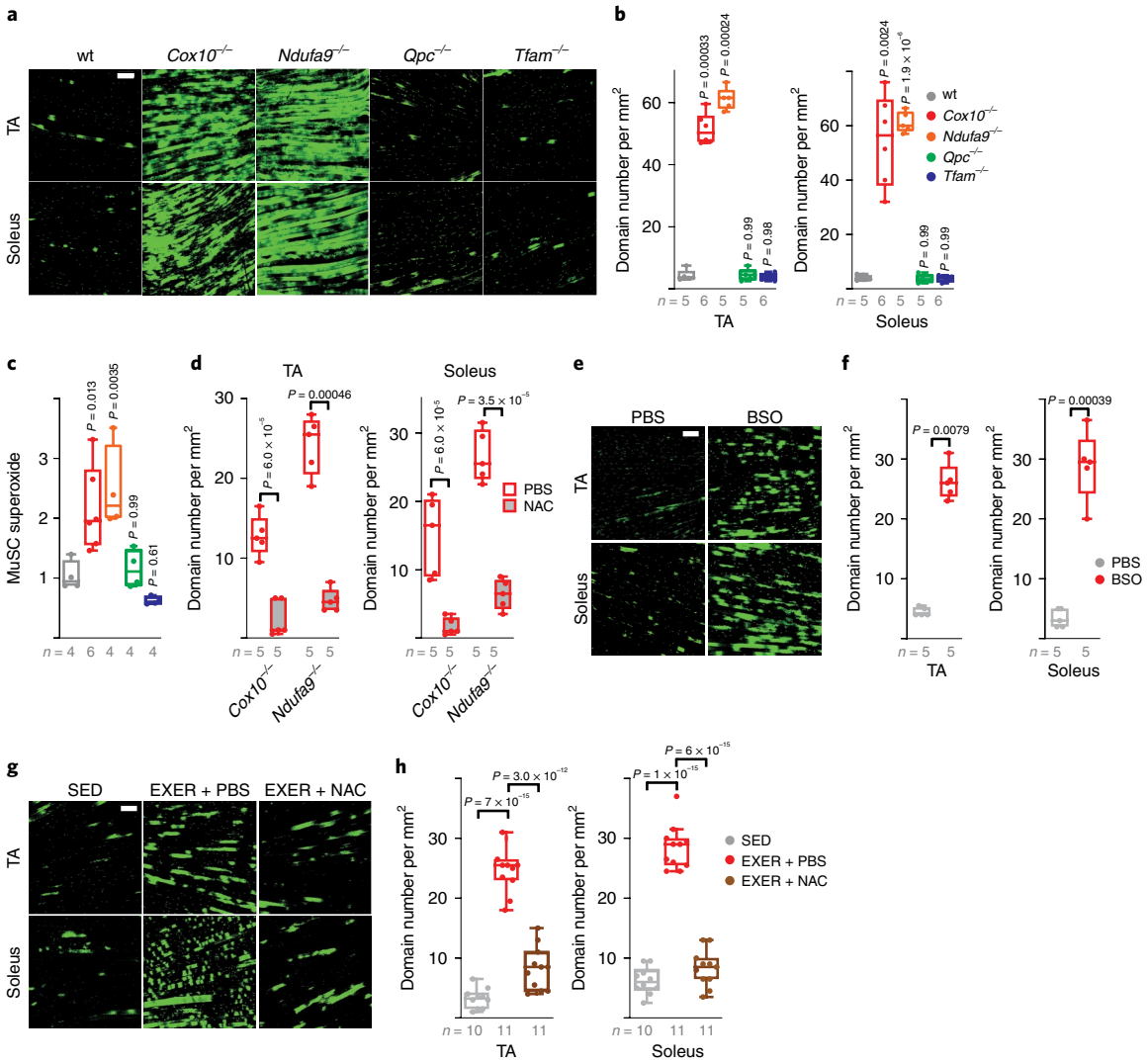

Fig. 3 | MuSC–myofiber fusion is regulated by ROS. a, Representative longitudinal images of mito-Dendra2 domains in TA and soleus muscles of mice of the indicated genotype (21 days after the first dose of tamoxifen). Scale bar, 200 µm. **b**, Quantitation of mito-Dendra2 domain numbers (normalized to muscle area) 21 days after the first dose of tamoxifen. *P* values reflect comparisons with the wt group. **c**, Relative superoxide levels in MuSCs of the indicated genotype 5 days after the first dose of tamoxifen. Same color scheme as **b**. *P* values reflect comparisons with the wt group. **d**, Mito-Dendra2 domain numbers (normalized to muscle area) in mice of the indicated genotype pretreated with vehicle (PBS) or NAC 5 days after the first dose of tamoxifen. **e**, Representative longitudinal images of mito-Dendra2 domains in TA and soleus muscles of mice treated with vehicle (PBS) or BSO for 21 days. Scale bar, 200 µm. **f**, Mito-Dendra2 domain numbers (normalized to muscle area) in mice treated with PBS or BSO for 21 days. **g**, Representative longitudinal images of mito-Dendra2 domains in TA and soleus muscles of sedentary (SED) mice, exercised mice treated with PBS (EXER+PBS) or exercised mice treated with NAC (EXER+NAC). Scale bar, 200 µm. **h**, Mito-Dendra2 domain numbers (normalized to muscle area) in mice of the indicated groups. Statistical significance was assessed using one-way ANOVA (**b**,**c**,**h**), two-way ANOVA (**d**), two-tailed *t* test (**f**) and two-tailed Mann–Whitney (**f**) tests with adjustments for multiple comparisons. Box plots indicate median values and interquartile ranges; whiskers are plotted using the Tukey method. The number of biological replicates in each group and *P* values are indicated. Experiments were repeated five or six times (**a**), five times (**e**) and 10–11 times (**g**), with similar results.

Fig. 6a), revealed a time-dependent increase in MuSC–myofiber fusion following tamoxifen administration, which corresponds with the slower kinetics of MuSC depletion in this protocol (Fig. 1d,e). This result was replicated in the single high-dose tamoxifen protocol (Extended Data Fig. 2a), where the more rapid depletion of MuSCs (Extended Data Fig. 2e,f) was accompanied by a corresponding rapid appearance of mito-Dendra2 domains within myofibers (Extended Data Fig. 6b). Thus, in two tamoxifen administration protocols with distinct kinetics, the appearance of mito-Dendra2 domains correlated in time with the depletion of MuSCs. In addition, experiments with an alternative reporter allele (*tdTomato*$^{f/f}$) replicated the induction of MuSC–myofiber fusion upon ETC dysfunction (Extended Data Fig. 6c,d).

As *Cox10* deletion was restricted to MuSCs in the above experiments, the induction of MuSC–myofiber fusion was likely due to cell-autonomous properties of these mutant MuSCs. Indeed, freshly isolated *Cox10*$^{-/-}$ MuSCs fused at increased frequencies with preformed C2C12 myotubes in vitro (Fig. 2c,d), despite defects in in vitro differentiation (Extended Data Fig. 6e). In addition, conditional genetic removal of the fusion machinery (*myomaker; Mymk*)[26] was sufficient to block fusion of *Cox10*$^{-/-}$ MuSCs in vivo (Fig. 2e and Extended Data Fig. 6f,g) and rescue the loss of MuSCs (Fig. 2f and Extended Data Fig. 6h), despite continued loss of ETC function (Extended Data Fig. 6i,j). Together, these results indicate that loss of *Cox10* in adult Pax7^{+} MuSCs triggers their depletion by inducing MuSC fusion into existing myofibers.

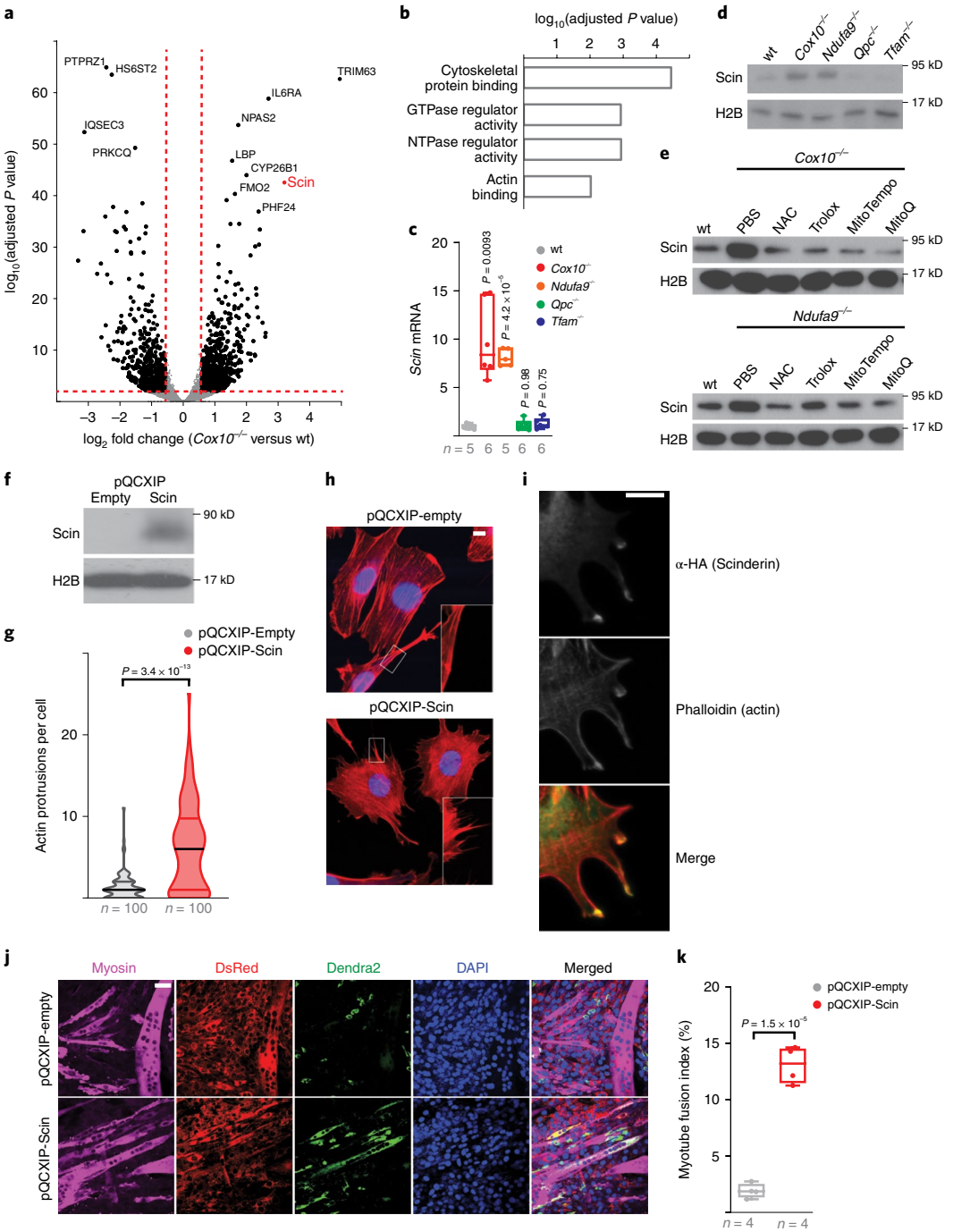

Fig. 4 | Scinderin induces actin network changes and MuSC–myotube fusion. a, Volcano plot of gene expression changes in *Cox10*$^{-/-}$ versus wild-type MuSCs. Log_2(fold change) is plotted against the log_{10}(adjusted *P* value) for each gene. **b**, Gene ontology analysis of upregulated genes in *Cox10*$^{-/-}$ MuSCs. **c**, Normalized *Scinderin* transcript levels in isolated MuSCs of the indicated genotype 5 days after the first dose of tamoxifen. *P* values reflect comparisons with the wt group. **d**, Scinderin protein levels in isolated MuSCs of the indicated genotype 5 days after the first dose of tamoxifen. Histone 2B (H2B) levels are shown as a loading control. **e**, Scinderin protein levels in isolated MuSCs of the indicated genotype and treatment 5 days after the first dose of tamoxifen. H2B levels are shown as a loading control. **f**, Scinderin protein levels in C2C12 cells infected with empty or Scinderin-overexpressing virus. H2B levels are shown as a loading control. **g**, Violin plots of actin protrusion numbers (per cell) for control and Scinderin-overexpressing C2C12 cells. **h**, Representative images of actin networks (stained by Acti-stain555 phalloidin, red) and nuclei (DAPI, blue) in control and Scinderin-overexpressing C2C12 cells. Scale bar, 10 µm. **i**, Scinderin (α-HA^{-} green) and actin (phalloidin; red) localization in cells overexpressing Scinderin. Scale bar, 10 µm. **j**, Representative images from an in vitro MuSC–myotube fusion assay; 10,000 Dendra2^{+} (green) freshly isolated control or Scin-overexpressing MuSCs were overlaid on DsRed^{+} (red) C2C12 myotubes and assessed for fusion with Myosin^{+} myotubes after 4 days. Cells were stained with myosin (magenta) and DAPI (blue). Scale bar, 50 µm. **k**, Quantitated myotube fusion indices for MuSCs of the indicated genotype. Statistical significance was assessed using one-way ANOVA (**c**), two-tailed Mann–Whitney test (**g**) or two-tailed *t* test (**k**). Box and violin plots indicate median values and interquartile ranges; whiskers are plotted using the Tukey method. The number of biological replicates per group and *P* values are indicated in the figure. Experiments were repeated three times (**h**,**i**) and four times (**j**), with similar results.

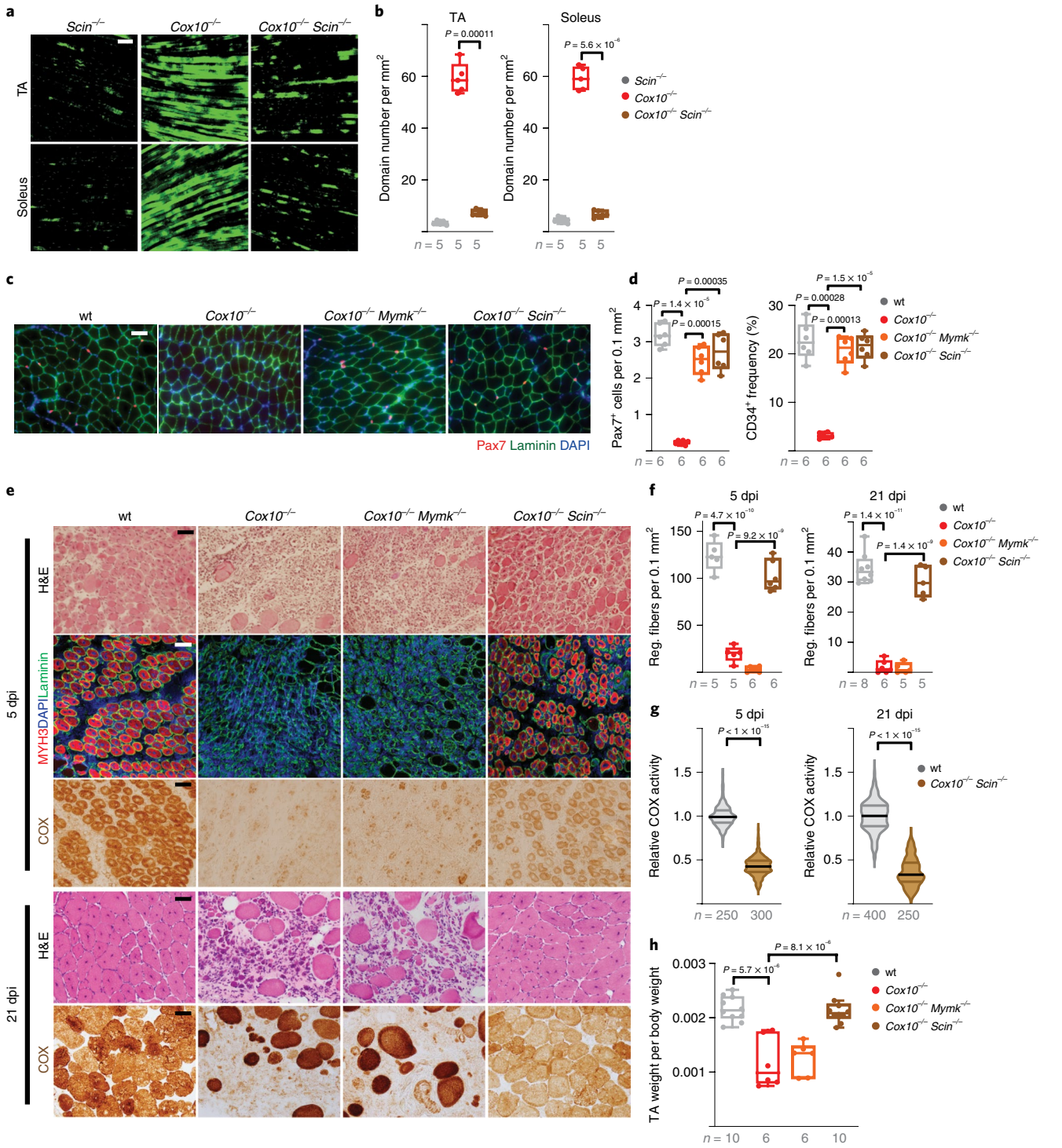

Fig. 5 | Scinderin is required for MuSC–myofiber fusion. a, Representative longitudinal images of mito-Dendra2 domains in TA and soleus muscles of mice of the indicated genotype 21 days after the first dose of tamoxifen. Scale bar, 200 µm. **b**, Mito-Dendra2 domain numbers (normalized to muscle area) 21 days after the first dose of tamoxifen. **c**, Representative images of endogenous Pax7$^+$ cells (red), laminin (green) and DAPI (blue) from TA cross sections from mice of the indicated genotype 21 days after the first dose of tamoxifen. Scale bar, 50 µm. **d**, MuSC (CD34$^+$) and Pax7$^+$ frequency in mice of the indicated genotype 21 days after the first dose of tamoxifen. **e**, Representative images of histology (H&E), MYH3$^+$ fibers (red) and complex IV activity (COX) in cross sections of TA muscles from mice of the indicated genotypes. Muscles were removed and assessed 5 or 21 days after $BaCl_2$ injury. For immunofluorescence staining, sections were stained with α-laminin (green), α-MYH3 (red) and DAPI (blue). Scale bar, 50 µm. **f**, Quantitation of regenerative fiber numbers (normalized to muscle area) in TA muscles 5 and 21 days after $BaCl_2$ injury. **g**, Normalized COX activity from regenerative myofibers 5 and 21 days after $BaCl_2$ injury. The number of analyzed fibers per group is indicated. **h**, TA weight (normalized to body weight) 21 days after $BaCl_2$ injury. Statistical significance was assessed using one-way ANOVA (**b**,**d**,**f**,**h**) or two-tailed Mann–Whitney (g) tests, with adjustments for multiple comparisons. Box and violin plots indicate median values and interquartile ranges; whiskers are plotted using the Tukey method. The number of biological replicates in each group and *P* values are indicated. Experiments were repeated five times (**a**), six times (**c**) and five to eight times (**e**), with similar results.

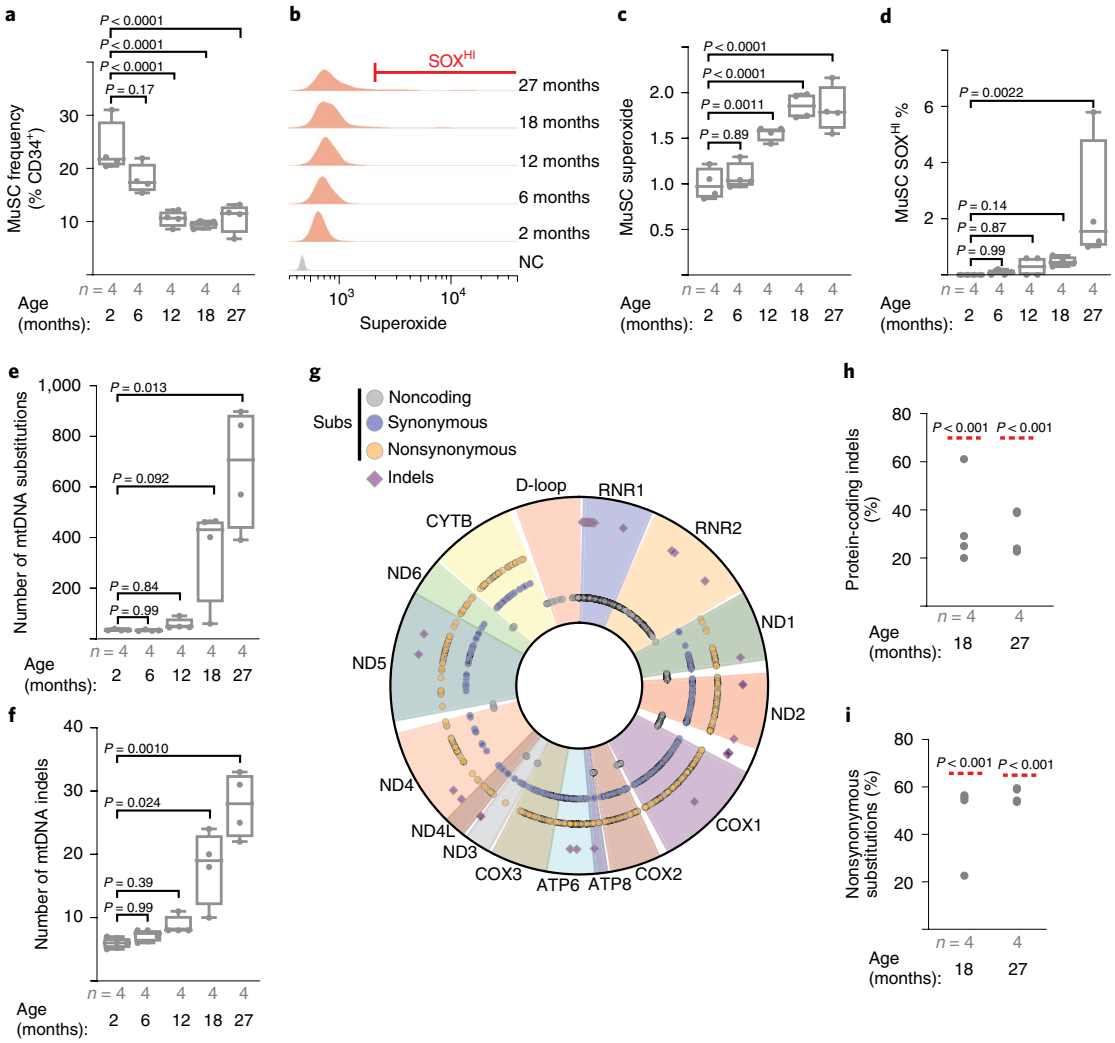

Fig. 6 | MuSCs accumulate mtDNA mutations with age. a, Quantitation of MuSC number (frequency of CD34+ cells) from wild-type mice of the indicated ages. **b**, Representative superoxide FACS profiles of MuSCs from mice of the indicated age. NC, unstained negative control. Gating for the SOX^{HI} (Superoxide^{HI}) population is indicated. **c**, Quantitation of mean superoxide levels in MuSCs of mice of the indicated age. **d**, Quantitation of SOX^{HI} population frequency from MuSCs of mice of the indicated age. **e**, Number of identified mtDNA substitutions from deep mtDNA sequencing of isolated MuSCs from mice of the indicated age. **f**, Number of identified mtDNA indels from isolated MuSCs of mice of the indicated age. **g**, Mapped positions of identified somatic mtDNA mutations (indels, noncoding, synonymous and nonsynonymous substitutions) in MuSCs from 27-month-old mice. **h**, Abundance of mtDNA protein-coding indels (as a percentage of total indels) observed in isolated MuSCs from mice of the indicated age. The expected frequency is indicated by the red line. **i**, Abundance of mtDNA nonsynonymous substitutions (as a percentage of total protein-coding substitutions) observed in isolated MuSCs from mice of the indicated age. The expected frequency is indicated by the red line. Statistical significance was assessed using one-way ANOVA (**a**,**c**), Kruskal–Wallis (**d**–**f**) and chi-squared (**h**,**i**) tests with adjustments for multiple comparisons. Box plots indicate median values and interquartile ranges; whiskers are plotted using the Tukey method. The number of biological replicates per group and *P* values are indicated.

MuSC–myofiber fusion is induced by ROS. Although subsets of quiescent MuSCs are known to occasionally fuse with myofibers in wild-type adult animals[27–29], the underlying mechanisms that induce these events are unknown. Our results thus far position ETC dysfunction as a critical trigger of MuSC–myofiber fusion. To test whether MuSC–myofiber fusion is a general consequence of ETC dysfunction, we next examined MuSC fate after loss of complex I function (*Ndufa9*$^{-/-}$), loss of complex III function (*Qpc*$^{-/-}$) or loss of mtDNA (complex I, III, IV and V; *Tfam*$^{-/-}$), using conditional alleles of these genes crossed with the *Pax7-Cre*$^{ERT2(Kardon)}$ driver and *D*^{f} lineage tracer. Tamoxifen-induced recombination of these alleles was sufficient to deplete target proteins and reduce ETC function in adult MuSCs (Extended Data Fig. 7a,b). Like *Cox10*$^{-/-}$ MuSCs, *Ndufa9*$^{-/-}$ MuSCs also acutely fused with existing myofibers, as indicated by the presence of Dendra2 domains within myofibers after tamoxifen administration (Fig. 3a,b). However, *Qpc*$^{-/-}$ or *Tfam*$^{-/-}$ MuSCs did not fuse with myofibers (Fig. 3a,b), indicating that not all modes of ETC dysfunction trigger MuSC–myofiber fusion. Correspondingly, deletion of *Ndufa9* (but not *Qpc* or *Tfam*) also resulted in acute depletion of MuSCs, similar to *Cox10* deletion (Extended Data Fig. 7c).

Different mechanisms of ETC dysfunction are associated with variable inductions in oxidative stress due to a differential ability to impact the redox-active prosthetic groups required for superoxide generation[30]. We observed elevated levels of cellular superoxide, as well as elevated mitochondrial superoxide and total ROS, in the *Ndufa9*$^{-/-}$ and *Cox10*$^{-/-}$ MuSCs, but not *Qpc*$^{-/-}$ or *Tfam*$^{-/-}$ MuSCs (Fig. 3c and Extended Data Fig. 7d). The lack of increased ROS in *Qpc*$^{-/-}$ and *Tfam*$^{-/-}$ MuSCs is consistent with previous experiments in other cellular systems[31,32]. The correlation between increased

ROS levels (Fig. 3c) and induced MuSC–myofiber fusion (Fig. 3a,b) suggests that elevated ROS may be a critical signal that initiates the fusion event. To test this idea, we treated mice with the antioxidant *N*-acetylcysteine (NAC) before and during tamoxifen-induced conditional deletion of *Cox10* or *Ndufa9*. NAC pretreatment lowered MuSC superoxide and mitoROS levels (Extended Data Fig. 7e) and inhibited MuSC–myofiber fusion in both genotypes (Fig. 3d), indicating that mitoROS elevation is associated with the induction of MuSC–myofiber fusion. Treatments with an alternative antioxidant (Trolox), as well as the mitochondrial targeted antioxidants MitoTempo and mitoquinone (MitoQ), were also sufficient to lower mitoROS levels in *Cox10*$^{-/-}$ and *Ndufa9*$^{-/-}$ MuSCs and block MuSC–myofiber fusion (Extended Data Fig. 7f,g). Thus, antioxidant treatment blocks the fusion of ETC-dysfunctional MuSCs with neighboring myofibers. Conversely, we induced elevated ROS in MuSCs of wild-type animals by systemic treatment with the pro-oxidant glutathione synthesis inhibitor (buthionine sulfoximine (BSO)) (Extended Data Fig. 7h). Daily BSO treatment (for 21 days) was sufficient to stimulate MuSC fusion to neighboring myofibers (Fig. 3e,f) and deplete MuSC levels (Extended Data Fig. 7i). Thus, induced pharmacologic elevations in systemic ROS correlate with enhanced MuSC–myofiber fusion.

Although the above genetic manipulations and pharmacologic (BSO) treatment resulted in substantial ETC dysfunction and/or oxidative stress, the physiological stresses experienced by MuSCs in wild-type conditions are likely less severe. We examined the effects of physiologic elevations in ROS, making use of a daily treadmill exercise regimen. Exercise regimens are known to be associated with transient oxidative stress in skeletal muscle tissue[33–37], although other pleiotropic effects are also present. Four weeks of daily treadmill running was sufficient to induce MuSC–myofiber fusion in hindlimb muscles of wild-type mice (Fig. 3g,h). Interestingly, this effect was blocked by daily treatment with NAC or other antioxidants (Fig. 3g,h and Extended Data Fig. 7j,k), indicating that the induced fusion was ROS dependent. Thus, physiologic elevations in ROS experienced by wild-type animals is associated with induction of MuSC–myofiber fusion.

Induction of Scinderin is required for MuSC–myofiber fusion. To identify mechanisms underlying the fusion of MuSCs with myofibers, we performed RNA sequencing (RNA-seq) analysis comparing wild-type and *Cox10*$^{-/-}$ MuSCs. We did not observe upregulation of Pax3 or other myogenic regulatory factors associated with MuSC activation in *Cox10*$^{-/-}$ MuSCs (Supplementary Table 1). Gene ontology analysis indicated that upregulated transcripts in *Cox10*$^{-/-}$ MuSCs were enriched for actin network binding and regulatory proteins (Supplementary Table 1 and Fig. 4a,b). Actin-dependent protrusions of the plasma membrane have been previously implicated in myoblast fusion[38,39], and analysis of the highest upregulated genes identified *Scinderin* (*Scin*), a member of the gelsolin family with actin network reorganization activity[40]. *Scinderin* mRNA and protein was upregulated in both *Cox10*$^{-/-}$ and *Ndufa9*$^{-/-}$ MuSCs, but not *Qpc*$^{-/-}$ or *Tfam*$^{-/-}$ MuSCs (Fig. 4c,d). Antioxidant treatment was sufficient to block *Scinderin* induction in *Cox10*$^{-/-}$ and *Ndufa9*$^{-/-}$ MuSCs (Fig. 4e).

In vitro, overexpression of Scinderin stimulated actin-rich protrusions of the plasma membrane in C2C12 myoblasts (Fig. 4f–h). Scinderin protein accumulated at sites of actin protrusion and colocalized with actin accumulation (Fig. 4i), suggesting a model whereby Scinderin induces actin cap formation at the plasma membrane to induce cellular protrusions and invasion into neighboring myofibers. We therefore infected primary wild-type MuSCs with Scin-expressing (or control) retrovirus and then overlaid them with preformed C2C12 myotubes. Although control MuSCs rarely fused with C2C12 myotubes, Scin-expressing cells often fused with preformed myotubes (Fig. 4j,k). The data implicate a model whereby Scinderin induces fusion of primary MuSCs via local activation of actin polymerization at the plasma membrane and subsequent membrane protrusion.

We next used a conditional knockout allele of *Scinderin*[41] to examine its in vivo role in MuSC fate and function. Deletion of *Scinderin* in Pax7^{+} MuSCs did not impair myofiber regeneration in response to injury (Extended Data Fig. 8a–c) or impair in vitro differentiation into myotubes (Extended Data Fig. 8d), indicating that *Scinderin* is not required for MuSC–MuSC fusion events necessary for new fiber formation. However, quiescent *Cox10*$^{-/-}$*Scin*$^{-/-}$ MuSCs no longer fused with existing myofibers at elevated rates in vivo (Fig. 5a,b), despite continued ETC dysfunction and elevated superoxide (Extended Data Fig. 8e–g), indicating that *Scinderin* is required for MuSC–myofiber fusion events induced by ETC dysfunction. Correspondingly, removal of *Scinderin* rescued the depletion of MuSCs mediated by loss of Cox10 (Fig. 5c,d). In addition, *Scinderin* was required for MuSC–myofiber fusion induced by systemic elevations in oxidative stress (BSO treatment or treadmill running) in wild-type animals (Extended Data Fig. 8h,i). Together, these data indicate a requirement for *Scinderin* in MuSC–myofiber fusion in response to multiple forms of oxidative stress.

MuSC–myofiber fusion prevents regeneration of damaged tissue. As described above (Figs. 1,2), *Cox10* deletion in MuSCs induces stem cell depletion, resulting in impaired myofiber regeneration. We therefore retested regenerative capacity in mice with *Cox10*$^{-/-}$*Scin*$^{-/-}$ mice, which retain MuSCs (Fig. 5c,d). In contrast to *Cox10*$^{-/-}$ animals, codeletion of *Scinderin* was sufficient to rescue regeneration from *Cox10*$^{-/-}$ MuSCs, resulting in the formation of de novo MYH3^{+} myofibers (Fig. 5e,f), as well as recovery of muscle mass at 3 weeks after injury (Fig. 5h). As expected, deletion of *Myomaker* did not rescue regeneration from *Cox10*$^{-/-}$ MuSCs, as *Myomaker* is required for MuSC–MuSC fusion[26,42] (Fig. 5e,f). Thus, the induction of MuSC–myofiber fusion and resulting depletion of MuSCs is responsible for the decline in regenerative capacity observed in mice with *Cox10*$^{-/-}$ MuSCs. However, de novo fibers formed from *Cox10*$^{-/-}$*Scin*$^{-/-}$ MuSCs exhibited significant mitochondrial impairment, as indicated by their depleted mitochondrial complex IV activity (Fig. 5e,g). Consistent with this, functional analysis performed 21 days after injury revealed significant defects in twitch and tetanic force generation (Extended Data Fig. 8j–m). Thus, in the absence of Scinderin-mediated MuSC–myofiber fusion, ETC-dysfunctional stem cells are retained in this experimental model and available to regenerate dysfunctional tissue.

Scinderin regulates MuSC functionality during aging. During aging, MuSCs are known to rapidly deplete, which is accompanied by elevations in ROS and metabolic signatures of ETC dysfunction[15,43]. Consistent with this literature, we assessed MuSC properties in a cohort of wild-type mice from 2 to 27 months of age, which revealed significant declines in MuSC numbers in early adulthood, as well as increased mitochondrial ROS in late adulthood (Fig. 6a–d). As mtDNA mutations have been observed to accumulate with age in various tissues, we purified MuSCs from wild-type mice of varying ages and performed deep sequencing of mtDNA genomes at high coverage (Extended Data Fig. 9a,b and Supplementary Table 2). Deep sequencing of MuSC mtDNA genomes revealed an age-dependent increase in the abundance of mtDNA mutations, including both substitutions and indels (insertions/deletions) (Fig. 6e,f and Extended Data Fig. 9c). Age-accumulating mutations occurred randomly throughout the mitochondrial genome, were predominantly of low allelic frequency and displayed mutational signatures consistent with mtDNA replicative errors[44,45] (Fig. 6g and Extended Data Fig. 9d,e). Thus, the murine MuSC population accumulates random mtDNA errors in late adulthood, which is correlated with the overall observed increases in superoxide levels. However, our

pooled sequencing analysis cannot distinguish allelic frequencies within individual cells, and thus, we cannot directly associate the presence of mtDNA mutations with elevated superoxide levels at the single-cell level. We noted that the observed frequencies of protein-coding indels, as well as nonsynonymous substitutions, were significantly lower than expected by random chance (Fig. 6h,i and Extended Data Fig. 9f), indicating that MuSCs select against dysfunctional mtDNA mutations during aging.

We therefore tested the role of MuSC–myofiber fusion in regulating MuSC properties during aging, making use of mice with conditional removal of *Scin* or *Mymk* in MuSCs starting at 6 weeks of age (Fig. 7a). As compared with wild-type animals, animals with *Scin*$^{-/-}$ MuSCs or *Mymk*$^{-/-}$ MuSCs exhibit increased MuSC numbers at multiple ages (12–30 months) (Fig. 7b and Extended Data Fig. 10a), indicating that the ongoing MuSC–myofiber fusion in wild-type animals significantly contributes to the depletion of MuSCs during physiologic aging. Assessment of mitochondrial ROS in 12-, 24- and 30-month-old MuSCs revealed that loss of *Scinderin* or *Myomaker* results in a significant accumulation of stem cells with elevated superoxide levels (Fig. 7c,d). Thus, in the absence of MuSC–myofiber fusion, MuSCs deplete more slowly with age and accumulate stem cells with elevated mitochondrial ROS.

Retention of dysfunctional MuSCs during aging potentially has consequences for the regeneration of healthy tissue. We inhibited MuSC–myofiber fusion via conditional deletion of *Scinderin* in MuSCs at 6 weeks of age and tested regeneration in young (2 months), middle-aged (12 months), older (24 months) and geriatric (30 months) animals. Loss of *Scinderin* had no functional consequences on regeneration in 2-month-old animals (Fig. 7e,f and Extended Data Fig. 8a-c). At 12 months of age, animals with *Scin*$^{-/-}$ MuSCs displayed intact regenerative capacity (Fig. 7e,f and Extended Data Fig. 10b), based on their ability to form new fibers. However, the regenerated tissue exhibited substantial defects, including reduced fiber size (Fig. 7f) and reduced complex IV activity, evident of mitochondrial dysfunction (Fig. 7g,h). Concomitant with this, regenerative fibers displayed significant increases in SDH activity (Fig. 7i,j), indicative of mitochondrial proliferation and accumulation commonly observed in the settings of muscular ETC dysfunction. These defects were retained in older (24-month-old) and geriatric (30-month-old) animals but were not observed in young (2-month-old) animals (Fig. 7e-j). Thus, deletion of *Scinderin* in MuSCs results in an age-dependent regenerative defect, likely due to the retention of MuSCs with elevated mitoROS that are unable to regenerate healthy tissue. In particular, the accumulating mitochondrial ETC dysfunction in aged MuSCs can be propagated to new myofibers if these cells are not removed by Scinderin-mediated MuSC–myofiber fusion.

Discussion

Our results indicate the consequences of mitochondrial damage in MuSCs. ETC dysfunction associated with elevated ROS triggers compromised MuSCs to directly fuse with existing myofibers. This mechanism is cell autonomous, as ETC-dysfunctional MuSCs are able to fuse to otherwise healthy myofibers; however, we cannot rule out potential contributions from signaling events within the receiving myofiber or the extracellular matrix, and this constitutes a limitation of our study. This self-removal of ETC-dysfunctional stem cells by MuSC–myofiber fusion contributes to the striking decline in MuSC numbers observed during aging (Fig. 8a,b) and limits the appearance of ETC-dysfunctional MuSCs in aged animals. Thus, our findings provide insight into mechanisms to attenuate loss and regulate MuSC health in aged individuals.

MuSC–myofiber fusion has been previously observed in wild-type mice. During early postnatal growth (up to postnatal day 21), MuSCs directly contribute to existing myofibers, resulting in an approximately fivefold increase in myonuclear numbers and an approximately sevenfold increase in cross-sectional area[46]. After this initial period, the contribution of MuSCs to myofibers is slow in sedentary animals but can be readily observed with lineage tracing studies[23,25]. In our experimental models of induced MuSC–myofiber fusion in adult animals, we did not observe changes in cross-sectional area or myonuclear number, consistent with the low number of MuSCs (~2–3% of total nuclei) present in adult tissue. Our results instead suggest that MuSC–myofiber fusion in adult muscle is typically reserved for stem cells accumulating high levels of oxidative stress. Our data do not indicate evidence of premature activation or differentiation in response to oxidative stress; however, it is possible that myogenic activation occurs very close in time to MuSC–myofiber fusion such that the induction of myogenic regulatory factors is difficult to detect, and this represents a limitation of our study.

We observe that although aged MuSCs accumulate mtDNA mutations, these cells display signatures of selection against dysfunctional mtDNA variants. Thus, in the absence of MuSC–myofiber fusion, ETC-dysfunctional MuSCs are retained and available to regenerate de novo tissue embodied by mitochondrial dysfunction (Fig. 8c). Thus, MuSC–myofiber fusion appears to be largely aimed towards preservation of a functional stem cell population, primed to regenerate healthy tissue, despite the decline in overall stem cell numbers. We speculate that the loss of stem cells does not substantially impact an organism's fitness until it is past reproductive age and suggest that this mechanism is optimized to promote healthy regeneration in response to injury in younger animals. However, future work will be needed to assess the consequences of contribution of ETC-damaged MuSCs into existing myofibers over long periods of time, which may directly impact the aging process.

Fig. 7 | Scinderin is required for regenerating healthy tissue in aged animals. a, Schematic of aging experiments in wild-type, *Mymk*$^{-/-}$ and *Scin*$^{-/-}$ mice. Recombination is induced in MuSCs of animals at 6 weeks of age via tamoxifen (TMX) administration, followed by aging and the indicated analysis at various time points (2, 12, 24 and 30 months of age). At each time point, MuSCs were analyzed in situ by FACS; in addition, TA muscles were injured by $BaCl_2$ and assessed for regeneration 21 days after injury. **b**, Pax7$^+$ cell numbers (normalized to muscle area) in animals of the indicated genotype and age. *P* values represent comparison with wild type for each age group. **c**, Representative FACS profiles of superoxide (SOX) levels in MuSCs isolated from animals of the indicated genotype and age. Gating for SOX^{HI} population is indicated. **d**, Quantitation of SOX^{HI} population frequency from MuSCs of mice of the indicated age and genotype. *P* values represent comparison with wild type for each age group. **e**, Representative images of histology (H&E) in cross sections of TA muscles from mice of the indicated genotypes and ages. Muscles were removed and assessed 21 days after $BaCl_2$ injury. Scale bar, 50 μm. **f**, Quantitation of fiber size from regenerative fibers (21 days after injury) in TA muscles of mice of the indicated genotypes and ages. **g**, Representative images of COX activity in cross sections of TA muscles from mice of the indicated genotypes and ages 21 days after $BaCl_2$ injury. **h**, Quantitation of relative COX activity in regenerative fibers (21 days after injury) from TA muscles of mice of the indicated genotypes and ages. **i**, Representative images of SDH activity in cross sections of TA muscles from mice of the indicated genotypes and ages 21 days after $BaCl_2$ injury. **j**, Quantitation of relative SDH activity in regenerative fibers (21 days after injury) from TA muscles of mice of the indicated genotype and ages. Statistical significance was assessed using two-way ANOVA (**b**,**d**) or two-tailed Mann–Whitney (**f**,**h**,**j**) tests, with adjustments for multiple comparisons. Box and violin plots indicate median values and interquartile ranges; whiskers are plotted using the Tukey method. The number of biological replicates in each group and *P* values are indicated. Experiments were repeated five to eight times (**e**,**g**,**i**), with similar results.

In addition, we observe that exercise (running) is sufficient to induce MuSC–myofiber fusion in wild-type mice, and this process can be regulated by systemic antioxidant treatment. ROS (induced by exercise) regulate the activation of a number of signaling pathways associated with improved insulin sensitivity and aerobic capacity, as well as muscle hypertrophy[47]. Indeed, a number of studies have suggested that antioxidant treatment can sometimes inhibit the beneficial effects of exercise training[48–53]. Our findings suggest that induction of MuSC–myofiber fusion may constitute part of the redox-dependent adaptation to exercise training, and

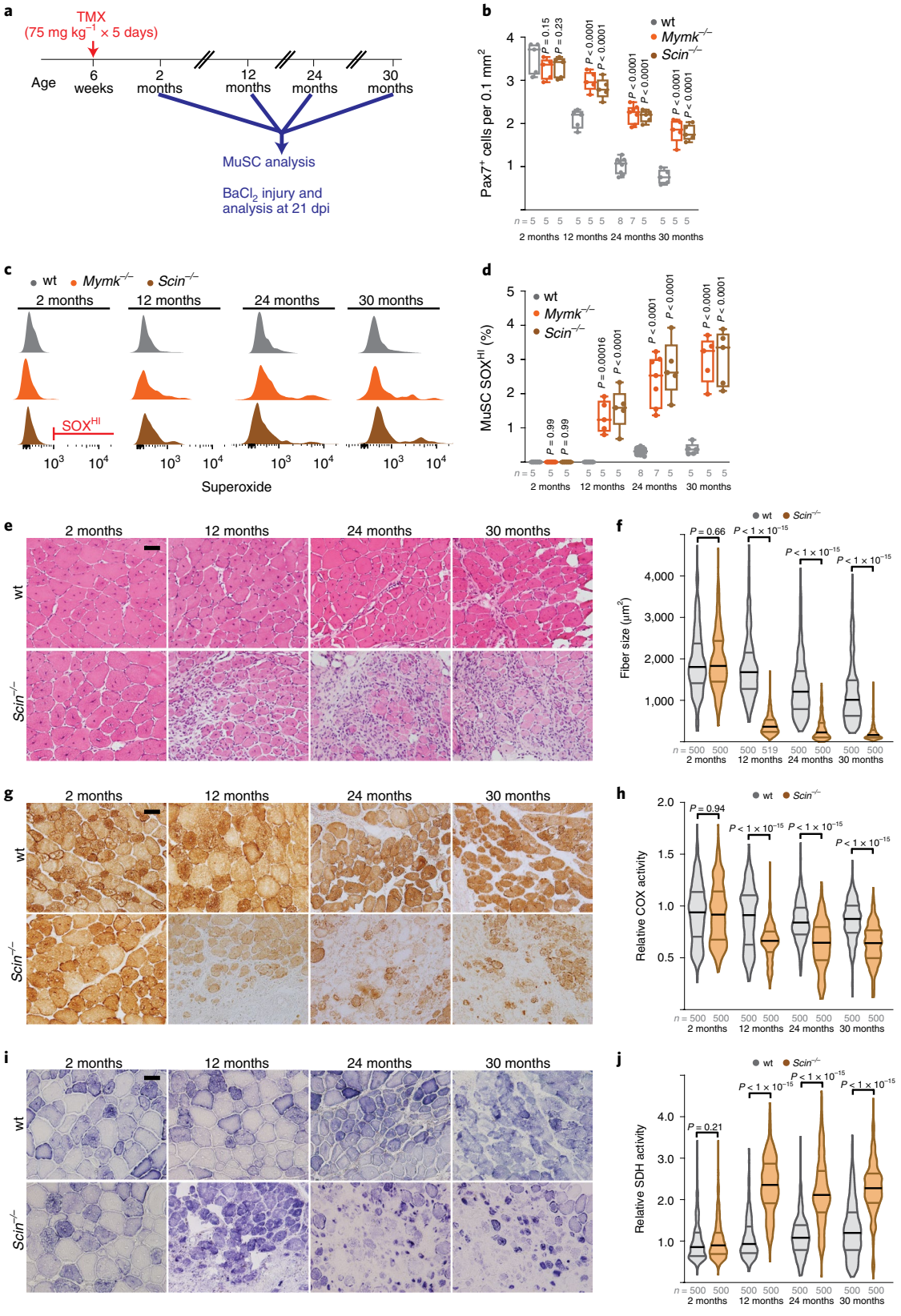

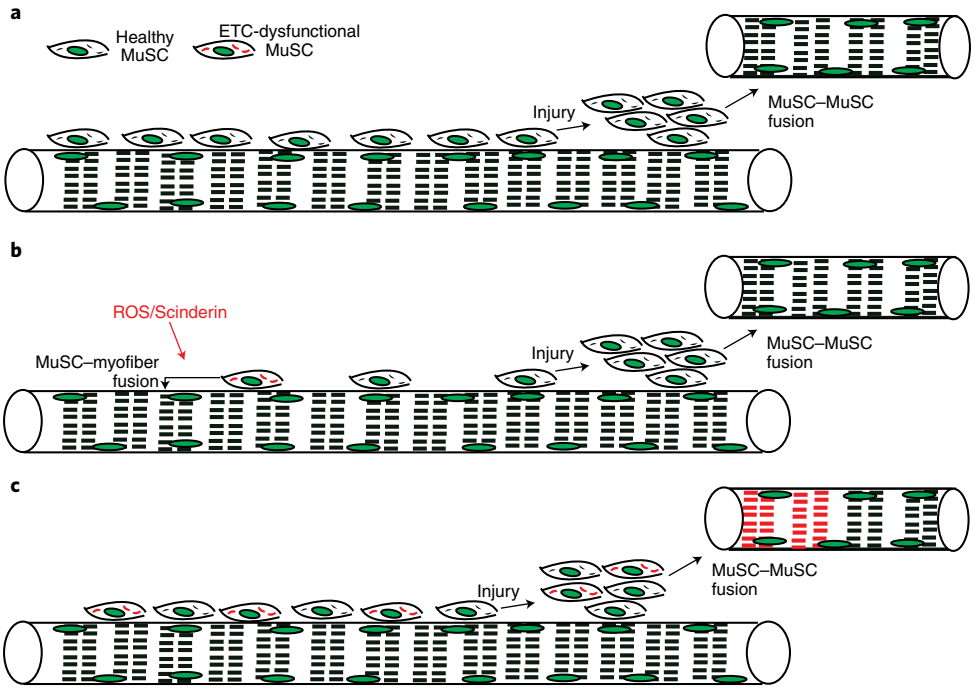

Fig. 8 | Proposed model: MuSC–myofiber fusion regulates removal of ETC-dysfunctional MuSCs during aging. a, In young wild-type animals, healthy MuSCs predominate and are competent to regenerate healthy myofibers in response to injury. **b**, In aged, wild-type animals, ETC-dysfunctional MuSCs (depicted with red mitochondria) are sensitive to elevated ROS and Scinderin levels and thereby induced to fuse into neighboring myofibers. In this manner, the remaining MuSC population contains healthy mitochondria and generates healthy myofibers in response to injury. **c**, In the absence of Scinderin during aging, MuSC–myofiber fusion is not available to remove ETC-dysfunctional MuSCs. In this setting, injury can trigger the activation, proliferation and fusion of damaged MuSCs, resulting in de novo myofibers with mitochondrial dysfunction.

future work will address the role of this phenomenon in contributing to muscle hypertrophy and activation of exercise-associated signaling pathways.

Our findings add to the accumulating literature on the relevance of mitochondrial dysfunction in stem cells. Maintenance of quiescence is well known to prevent stem cell exhaustion in numerous tissue systems, and quiescent stem cells typically require protective mechanisms to protect them from damage as they age. In response to nuclear DNA damage, stem cells are dependent on DNA repair pathways to maintain functionality[54,55]. In contrast, mtDNA damage is not associated with a robust repair mechanism. We found that MuSCs retain a unique mechanism to cope with ETC deficiency, and it will be intriguing to investigate whether other stem cell compartments respond to mtDNA damage in a distinctive manner and how this mechanism interplays with other quality-control organelle mechanisms (e.g. mitophagy). A recent report from in vitro cultured mammary stem cells suggests that young mitochondria are preferentially sequestered into daughter cells to promote stemness, whereas retention of old mitochondria promotes differentiation[56], and our findings add to the general model that damaged mitochondria hamper maintenance of a quiescent stem cell population.

The identification of *Scinderin* as a specific regulator of MuSC–myofiber fusion allows the dissection of MuSC–myofiber fusion separately from MuSC–MuSC fusion events (associated with injury-induced regeneration). Indeed, our results suggest that MuSC–myofiber fusion requires the low levels of Myomaker found in quiescent MuSCs, although it is possible that Myomaker expression is induced immediately before fusion. Our data thereby indicate that there are mechanistic differences between these two modes of cell fusion, and it will be important in the future to evaluate the biophysical differences in membrane dynamics therein. More generally, the observation that dysfunctional stem cells are induced to fuse with existing tissue suggests opportunities to target age-associated pathology via regulation of stem cell–tissue fusion events.

Methods

Mice. Throughout this study, all genotypes refer to animals with conditional (floxed (f)) alleles, targeted to the MuSC population. *Cox10*$^{f/f}$ (strain 024697), Pax7-Cre$^{ERT2(FAN)}$ (strain 012476), Pax7-Cre$^{ERT2(KARDON)}$ (strain 017763), C57BL/6 (strain 000664), *tdTomato*$^{f/f}$ (strain 007914) and *mito-Dendra2*$^{f/f}$ (strain 018385) mice were purchased from The Jackson Laboratory. For lineage tracing experiments, we exclusively used the *Pax7-Cre*$^{ERT2(Kardon)}$ allele, as the *Pax7-Cre*$^{ERT2(Fan)}$ allele displayed leaky recombination in the absence of tamoxifen. The generation of *Qpc*$^{f/f}$, *Tfam*$^{f/f}$, *Mymk*$^{f/f}$ and *Scin*$^{f/f}$ conditional knockout mice was described previously[31,41,42,57].

The *Ndufa9*$^{f/f}$ conditional knockout mouse was generated at the Children's Research Institute Mouse Genome Engineering Core using the Easi-CRISPR workflow[58]. sgRNAs surrounding exon 4 of *Ndufa9* were selected by cross-referencing CHOPCHOP, the MIT CRISPR Design Website, and the CRISPR-Cas9 guide checker tool (Integrated DNA Technologies) (Supplementary Fig. 1a). CRISPR-Cas9 crRNAs and the Megamer single-stranded DNA fragment homology-directed repair template were purchased from Integrated DNA Technologies. Animals were screened for insertion of the conditional allele by PCR, and correct targeting was confirmed by Sanger sequencing. Genotyping primers for *Ndufa9*$^{f/f}$ mice are provided in Supplementary Table 3.

All mice were maintained on C57BL6 backgrounds, except *Ndufa9*$^{f/f}$ mice, which were on a mixed background. Both male and female mice were used in all experiments; sex-specific differences were not present, and male and female mice were analyzed together. Six- to 8-week-old mice were used for all experiments, except in Figs. 6 and 7, where ages are indicated. All mice were housed in the Animal Resource Center at the University of Texas Southwestern Medical Center under a 12-h light/dark cycle and fed ad libitum. All animal protocols were approved by the University of Texas Southwestern Institutional Animal Care and Use Committee (protocol 101323), and all relevant guidelines were adhered to while carrying out this study.

Generation and characterization of *Ndufa9*$^{f/f}$ mouse embryonic fibroblasts (MEFs). Embryonic day 13.5 embryos were collected from *Ndufa9*$^{f/f}$ or wild-type pregnant females after carbon dioxide asphyxiation and cervical dislocation. Embryos were dissected to remove the head and red organs, minced with a sterile scalpel and digested with trypsin for 45 min at 37 °C. Digested embryos were subsequently collected in DMEM (Sigma-Aldrich, D6429) with 10% FBS, 2 mM

L-glutamine and 1% penicillin/streptomycin and plated to tissue culture flasks that were pretreated with gelatin (10 ml 0.1% gelatin/H_2O solution per 75-cm^2 surface area for 1 h at 37 °C). *Ndufa9*$^{+/+}$ or *Ndufa9*$^{f/f}$ MEFs were immortalized by transduction with lentiCRISPRv2 expressing an sgRNA targeting Trp53 at a multiplicity of infection of ~0.5 (visual estimation) and subsequently selected with 5 μg ml^{-1} puromycin for 4 days. Approximately 5×10^6 immortalized MEFs were incubated in 1 ml media with 25 μl Ad5-CMV-EGFP or Ad5-CMV-CreEGFP adenovirus (University of Iowa Viral Vector Core; VVC-U of Iowa-4 and VVC-U of Iowa-1174, respectively) for 10 min at room temperature before being plated to tissue culture dishes. After transduction with EGFP or CreEGFP adenovirus, MEFs were continuously cultured in media containing 1 mM sodium pyruvate and 100 μg ml^{-1} uridine; 48 h later, transduced MEFs were sorted at the UT Southwestern Children's Research Institute Moody Foundation Flow Cytometry Facility, and GFP$^+$ cells were selected. Transduced cells were verified for genotype by PCR analysis (Supplementary Fig. 1b) and western blot (Supplementary Fig. 1c).

An Agilent Seahorse XFe96 Analyzer was used for cellular oxygen consumption measurements of *Ndufa9*$^{+/+}$ and *Ndufa9*$^{f/f}$ MEFs (Supplementary Fig. 1d). MEFs were plated at 10,000 cells per well in 80 μl media and allowed to adhere overnight. The following day, cells were washed twice with 200 μl per well assay medium (DMEM (Sigma-Aldrich, D5030) with 10 mM glucose, 2 mM L-glutamine, 1 mM sodium pyruvate and 1% penicillin/streptomycin), and 150 μl assay medium was added to each well after the second wash. Cells were transferred to a 37 °C, CO_2-free incubator for 1 h. Standard calibration and baseline oxygen consumption measurements were performed using a 3-min 'mix'/3-min 'measure' cycle with three measurements recorded at baseline and after injection of each compound. The following inhibitors were used: 2 μM oligomycin, 3 μM CCCP and 3 μM antimycin A. Data collection was performed with WAVE (v.2.4.1.1) software.

MuSCs isolation via FACS. Murine MuSC isolation was adapted from a published protocol[59]. Following carbon dioxide asphyxiation and cervical dislocation, skeletal muscle was rapidly dissected and sequential digested with Collagenase II (1 h) and Dispase (30 min) at 37 °C. Mononucleated cells were collected through a 70-μm cell strainer and suspended in HBSS with 2% horse serum (Gibco, 16050114). Cells were then incubated with the following antibodies on a rotator at 4 °C for 30 min: APC-conjugated anti-mouse CD31 (BioLegend, clone MEC13.3, 102510, 1:100), APC-conjugated anti-mouse CD45 (BioLegend, clone 30-F11, 103112; 1:100), PerCP-Cy5.5–conjugated anti-mouse Sca-1 (Invitrogen, clone D7, 45598182, 1:100) and biotin-conjugated anti-mouse CD34 (Invitrogen, clone RAM34, 13034181, 1:100). After incubation, cells were washed twice and then incubated with phycoerythrin (PE)/Cy7–conjugated streptavidin (BioLegend, 1:100, 405206) on a rotator at 4 °C for 20 min. Cells were washed twice and then suspended with 2% horse serum in HBSS with DAPI. Quiescent MuSCs (Extended Data Fig. 9a) were identified as the CD34$^+$, CD31$^-$, CD45$^-$, DAPI$^-$ and Sca-1$^-$. For isolation of mito-Dendra2$^+$ cells, mononucleated cells were resuspended with 2% horse serum in HBSS with DAPI, and GFP$^+$, DAPI$^-$ cells were isolated. Purity was confirmed by immunofluorescence staining for Pax7. All sorting was performed at the Moody Foundation Flow Cytometry Facility on a FACS Aria flow cytometer (BD Biosciences). Data were collected by FACSDiva (v.8.0.2, BD Biosciences) software and analyzed using FlowJo (v10.6.1) software.

ROS and mitochondrial membrane potential (ΔΨm) analysis. For ROS analysis, MuSCs were resuspended in HBSS with 5 μM final concentration Superoxide Detection reagent (total superoxide levels; Enzo Life Sciences, 51010), 5 μM final concentration mitoSOX (mitochondrial superoxide levels, Thermo Fisher, M36008), or 1 μM final concentration mitoROS (mitochondrial total ROS levels; Cayman Chemical, 701600) and then incubated at 37 °C for 30 min. After incubation, cells were washed and resuspended in HBSS with DAPI, followed by immediate FACS analysis.

For mitochondrial membrane potential analysis, MuSCs were isolated at 5 days after the first dose of tamoxifen and resuspended in mitochondrial assay buffer with the indicated mitochondrial substrates and inhibitors (see below for recipes). Cell suspensions were incubated at 37 °C for 30 min. After incubation, cells were washed and then suspended in HBSS with DAPI.

The mitochondrial assay buffer contained 220 mM mannitol, 70 mM sucrose, 10 mM KH_2PO_4, 5 mM $MgCl_2$, 2 mM HEPES and 1 mM EGTA, pH 7.4, supplemented with fresh TMRE (Invitrogen, T669; final concentration, 150 nM) and fresh PMP reagent (Agilent, 102504-100; final concentration, 3 nM).

Pyruvate/malate buffer contained mitochondrial assay buffer supplemented with 10 mM pyruvate and 5 mM malate, pH 7.4.

Inhibitor concentrations were 5 μM for CCCP and 5 μM for rotenone.

RNA isolation and sequencing. Total RNA was purified from FACS-isolated MuSCs using the RNeasy Micro Kit (Qiagen, 74004) according to manufacturer's instructions. Library preparation was performed using the SMARTer stranded pico input total RNA-seq kit (Takara Bio, 634411) following the manufacturer's instructions. Next-generation sequencing was performed using an Illumina NextSeq 500 by the Children's Research Institute's Sequencing Facility at UT Southwestern Medical Center. RNA-seq analysis was performed on BICF RNASeq Analysis Workflow (ssh://git@git.biohpc.swmed.edu/BICF/Astrocyte/rnaseq.git) provided by the UTSouthwestern Bioinformatics Core Facility. Gene ontology analysis was performed using DAVID (https://david-d.ncifcrf.gov/home.jsp). Summary statistics are provided in Supplementary Table 1, and raw RNA-seq data have been deposited to the NCBI GEO under accession number GSE180867.

mtDNA sequencing and analysis. Total DNA was purified from FACS-isolated MuSCs using the QIAamp DNA Micro kit (Qiagen, 56304). mtDNA sequences were enriched by rolling circle amplification using the Repli-G Mitochondrial DNA kit (Qiagen, 151023), following manufacturer protocols[60]. Library preparation was performed using the Nextera XT DNA Library Preparation Kit (Illumina, FC-131-1096) following manufacturer instructions. Paired-end sequencing (2 × 150 bp) was performed using an Illumina NextSeq 500 by the Children's Research Institute's Sequencing Facility at UT Southwestern Medical Center. Sequencing analysis was performed using an in-house pipeline. Briefly, sequencing reads were checked and trimmed for quality control using FastQC 0.11.8 and TrimGalore 0.6.4. Trimmed reads were mapped to the *Mus musculus* mitochondrial genome GRCm38 using MapSplice2 2.2.1, and then paired-end reads were deduplicated (Picard 2.23.1) and quality filtered (SAMtools 1.9.0) to include high-confidence mappings. Per-base sequencing depth and point mutations were assessed using bam-readcount 0.8.0 for the quality-filtered mapped reads. Mean coverage was 7,676× (range = 5,088–9,601×) (Extended Data Fig. 9b and Supplementary Table 2). To avoid false positives and mtDNA-derived nuclear psueodgenes, variants (substitutions and indels) were called when detected on both heavy and light strands with greater than 50 supporting reads and greater than 0.5% allelic frequency. Substitutions displayed a bias towards C>T and T>C transitions (Extended Data Fig. 9e), consistent with previous mtDNA mutational signatures observed in human populations[44,61], and were predominantly of low allelic frequency (Extended Data Fig. 9d). Large deletions were determined using the noncanonical junction detection mode of MapSplice2. The deletion frequency was calculated as:

$$\frac{\text{Supports}}{\text{Supports} + \text{MeanCoverage\_by\_FullAlignments}}.$$

Here, supports is the number of read pairs supporting a large deletion, and MeanCoverage_by_FullAlignments is the average read depth using all reads that mapped to the region with no detected deletion. Junction coordinates for the deletion were extracted by regtools 0.5.1, and bedtools 2.29.2 was used to calculate MeanCoverage_by_FullAlignments from the nonjunction reads. A single large-scale deletion was noted (7,193–8,150, encompassing parts of the Cox2, ATP8, ATP6 and Cox3 genes) in MuSCs from older animals (Extended Data Fig. 9b,c (red arc)).

Statistical analysis of indel and nonsynonymous substitution frequency was performed based on a published method[62]. Briefly, expected frequencies of indels were calculated based on the relative size of protein-coding (69.88%) and non–protein-coding (30.12%) regions in the mouse mitochondrial genome. For expected frequencies of nonsynonymous substitutions, we took into account the observed mutational signatures at 18 and 27 months of age.

Age (months)	A>C	A>G	A>T	C>A	C>G	C>T
18	0.0058	0.18	0.072	0.011	0.00072	0.28
27	0.0044	0.23	0.063	0.0056	0.0015	0.22

Age (months)	G>A	G>C	G>T	T>A	T>C	T>G
18	0.097	0.00	0.0058	0.014	0.33	0.00
27	0.071	0.00037	0.0030	0.012	0.38	0.00

For each of the 13 protein-coding genes, we simulated 300,000 substitutions of the wild-type mouse sequence (extracted from the mouse reference mitochondrial genome: NC_005089) based on the above mutational signature. For each simulation, we calculated the frequency of nonsynonymous and synonymous substitutions. Statistical significance of the observed number of protein-coding indels and nonsynonymous substitutions was then calculated using a chi-squared test (Fig. 6h,i and Extended Data Fig. 9f). Summary statistics are provided in Supplementary Table 2, and raw mtDNA-seq data are available at the NCBI GEO website under accession GSE180953.

Quantitative real-time PCR. Total RNA was extracted from sorted MuSCs using the RNeasy Micro Kit (Qiagen, 74004) following the manufacturer's instructions. After RNA isolation, real-time RT-PCR were performed with Luna Universal One-Step RT-qPCR Kit (New England Biolabs, E3005) following the manufacturer's protocol, on a CFX384 Real-Time System (SN027118, Bio-Rad). Transcript levels were normalized to β-2 microglobulin using the $2^{-\Delta\Delta CT}$ method[63]. For genomic PCR reactions, genomic DNA was purified from isolated MuSCs using phenol-chloroform extraction. Oligonucleotide sequences are provided in Supplementary Table 3.

Western blot analysis. For C2C12 myoblasts and MEFs, trypsinized cells were spun down, washed with PBS and resuspended in RIPA buffer (Thermo Scientific, 89900) supplemented with protease inhibitor cocktail (Roche, 11873580001), and put on ice for 30 min. Lysates were spun down at 12,000 *g* at 4 °C for 10 min. Protein concentrations were quantitated with the DC protein assay (Bio-Rad, 5000112). For MuSCs, 50,000 FACS-isolated cells were collected in PBS, spun down and resuspended in 50 µl RIPA buffer and processed as above. The following antibodies were used: Cox10 (Abcam, ab84053, 1:1,000), Qpc (Proteintech, 14975-1-AP, 1:1000), TFAM (Santa Cruz Biotechnology, sc-166965; 1:1,000), Scin (Santa Cruz Biotechnology, sc-376136; 1:1,000), Ndufa9 (Thermo Fisher, 459100; 1:2,000), cleaved caspase-3 (Cell Signaling Technology, 9664; 1:1,000), β-actin (Cell Signaling, 4970; 1:5,000) and histone H2B (Santa Cruz Biotechnology, sc-515808; 1:1,000). Uncropped western blot images are provided in Supplementary Figs. 2,3.

Mouse injections. Tamoxifen (Cayman Chemical, 132585) was dissolved in corn oil (Sigma-Aldrich, C8267). For most experiments, 75 mg kg^{-1} body mass was administered by intraperitoneal injection to 6- to 8-week-old mice once per day for five consecutive days. For experiments shown in Extended Data Fig. 2, a single dose of 200 mg kg^{-1} body mass of tamoxifen was administered by intraperitoneal injection to 6- to 8-week-old mice. Mice were euthanized and tissue removed at various time points after tamoxifen administration (3 h to 9 months) as indicated.

For BSO (Cayman Chemical, 14484500) administration experiments, mice were first treated with tamoxifen for 5 days (as above). Starting the day after the fifth tamoxifen administration, BSO was administered at 4 mmol per kilogram body mass once per day by intraperitoneal injection for 21 days. Mice were then euthanized, and tissue was removed for analysis.

The following antioxidants were administered: NAC (Sigma-Aldrich, A7250; 200 mg kg^{-1} per day), Trolox (Sigma-Aldrich, 238813; 50 mg kg^{-1} per day), MitoQ (Biovision, B1309; 10 mg kg^{-1} per day) or mitoTEMPO (Cayman Chemical, 1662125; 1 mg kg^{-1} per day). Mice were treated with antioxidants once per day by intraperitoneal injection for 7 days. On days 3–7, tamoxifen (75 mg kg^{-1}) was administered by intraperitoneal injection once per day. Mice were euthanized and tissue was removed 1 day after the fifth dose of tamoxifen (7th dose of antioxidant).

Muscle injury experiments. For cryoinjury experiments, 6- to 8-week-old mice were pretreated with tamoxifen (75 mg kg^{-1} intraperitoneal injection once per day for 5 days) as above. Two days after the last tamoxifen injection, a cryoinjury protocol was performed. Mice were anesthetized with isoflurane. A single incision was made in the skin overlying the TA, and a metal probe (0.5 mm diameter) was cooled in liquid nitrogen and then applied directly onto the exposed TA for 10 s. Following the cryoinjury, the wound was closed with size 7–0 polyamide threads (Ethicon, 1647G). Postoperative analgesia with meloxicam (Sigma-Aldrich, M3935, 2 mg kg^{-1} per 24 h) was administered subcutaneously once per day for 2 days. Mice were euthanized and tissue removed between 2 and 14 days after injury as indicated.

For $BaCl_2$ (Alfa Aesar, 0361-37-2) injury experiments, 6- to 8 week-old mice were pretreated with tamoxifen (75 mg kg^{-1} intraperitoneal injection once per day for 5 days) as above. Two days following the last tamoxifen injection, a muscular $BaCl_2$ injury was administered. Mice were anesthetized with isoflurane. TA muscles were directly injected with 50 µl of 1.2 % $BaCl_2$ (in sterile saline) using a sterile 29G needle. Postoperative analgesia with meloxicam (Sigma-Aldrich, 2 mg kg^{-1} per 24 h) was administered subcutaneously once per day for 2 days. Mice were euthanized and tissue removed between 2 and 21 days after injury as indicated.

Treadmill running experiments. For long-distance running experiments, mice were randomized to different treatment groups (sedentary, exercise + PBS or exercise + antioxidant). Mice were first administered tamoxifen for 5 days (as described above). On the day after the fifth tamoxifen administration, mice were acclimated to the treadmill (Columbus Instruments) by running 30 min per day for 3 days at slow speeds (up to 10 m min^{-1}). After the acclimation period, mice were run daily on a treadmill with mild electrical stimulus and 0° inclination. The treadmill speed was set at 15 m min^{-1}, and running was conducted 30 min per day for 6 days per week for 4 weeks. Exercised mice were treated with subcutaneous injection of NAC (200 mg kg^{-1} per day), Trolox (50 mg kg^{-1} per day), MitoQ (10 mg kg^{-1} per day), mitoTEMPO (1 mg kg^{-1} per day) or PBS 6 h before each treadmill run.

TA muscle force measurement in situ. TA muscle force was measured in animals at 21 days after $BaCl_2$ injury using a protocol (http://www.treat-nmd.eu/downloads/file/sops/dmd/MDX/DMD_M.2.2.005.pdf). Briefly, mice were anesthetized with isoflurane, and the hindlimb was secured. The sciatic nerve was exposed in the posterolateral thigh and clamped to a custom electrode. The TA muscle was exposed, and the distal tendon was severed and attached to a force transducer via a suture (Grass Instruments, FT03-E). During measurement, the TA muscle and nerve were kept moist with 37 °C saline. The TA muscle was stimulated via the sciatic nerve using a pulse generator (Siglent Technologies, SDG2042X), and the resulting force output from the force transducer was recorded via a digital acquisition board (Dataq Instruments, DI-1110) using WinDaq software (v.3.0.7). The stretched muscle length was optimized to achieve maximal force, followed by optimization of supramaximal stimulation voltage (typically 3–4 V) and pulse duration (typically 0.3–0.4 ms). Maximal twitch force was collected for 8–10 trials and normalized by muscle cross-sectional area. Following measurement of twitch force, the force–frequency relationship was measured over stimulation frequencies from 5 to 125 Hz, at supramaximal stimulation. Data were analyzed and plotted in MATLAB (MathWorks).

Skeletal muscle clearing and deep tissue imaging. The PEGASOS tissue clearing method[64] was used for whole-mount muscle clearing before deep tissue imaging. Mice were anesthetized, transcardially perfused with 50 ml ice-cold heparin PBS and then 50 ml 4% PFA. Muscles were dissected and immersed in 4% PFA at room temperature for 24 h. Subsequently, samples were incubated with decolorization solution (25% (v/v in H_2O) Quadrol (Sigma-Aldrich, 122262) for 2 days at 37 °C with gentle shaking. Next, delipidation was performed at 37 °C with gentle shaking using the following gradient of tert-butanol (tB) solutions over 2 days: (1) 30% tB (Sigma-Aldrich, 471712) solution (70% v/v H_2O, 27% v/v tB and 3% w/v Quadrol), (2) 50% tB solution (50% v/v H_2O, 47% v/v tB and 3% w/v Quadrol) and (3) 70% tB solution (30% v/v H2O, 67% v/v tB and 3% w/v Quadrol).

Next, samples were immersed into dehydration solution consisting of 70% tB, 27% (v/v) poly(ethylene glycol) methyl ether methacrylate average Mn500 (PEG MMA500) (Sigma-Aldrich, 447943) and 3% (w/v) Quadrol at 37 °C for 2 days. Samples were then incubated in clearing medium (75% (v/v) benzyl benzoate (Sigma-Aldrich, B6630), 22% (v/v) PEG MMA500 and 3% (w/v) Quadrol) at 37 °C with gentle shaking until they achieved fully transparency. Muscles were imaged on a Zeiss LSM780 Inverted confocal microscope, and data were collected with Zeiss Zen (v.14.0.0.201) software. Imaris software (Bitplane) was used to create Supplementary Videos 1–3.

Mito-Dendra2 and tdTomato myofiber domain imaging. Myofiber domains were imaged and quantitated similar to previous studies[25]. Briefly, acutely dissected skeletal muscle was immediately fixed in formalin for 3–4 h at room temperature, followed by overnight at 4 °C. Muscles were rinsed with PBS and then mounted in a glass-bottom dish (MatTek, P35G-1.5–14-C). Muscles were imaged using a Zeiss LSM780 inverted confocal microscope and analyzed with ImageJ software.

Histology analysis of skeletal muscle. Following CO_2 asphyxiation and cervical dislocation, the indicated skeletal muscles were rapidly dissected and then freshly frozen in liquid nitrogen–cooled 2-methylbutane, before embedding in O.C.T compound (Thermo Fisher Scientific, 23-730-571). Sections (10 µM) were cut on a cryostat (Leica, CM3050S). For H&E staining, slides were prepared following the protocol from the TREAT-NMD website (http://www.treat-nmd.eu/downloads/file/sops/cmd/MDC1A_M.1.2.004.pdf). For COX/SDH staining, slides were stained for COX activity and SDH activity based on standard operating protocols (https://neuromuscular.wustl.edu/pathol/histol/cox.htm; https://neuromuscular.wustl.edu/pathol/histol/SDH.pdf). β-Galactosidase staining was performed using a β-galactosidase staining kit (Cell Signaling Technology, 9860) following the manufacturer's instructions. Sections were imaged using an Olympus IX83 microscope and analyzed with Image J software (National Institutes of Health) to calculating myofiber numbers and COX/SDH intensity.

Immunofluorescence protocols. For muscle sections, freshly frozen 10-µm sections (prepared as above) were fixed in formalin at room temperature for 5 min and then blocked with blocking buffer (0.25% Triton X-100 (Sigma-Aldrich, X100)) and 10% goat serum (Gibco, 16210064) in PBS at room temperature for 1 h. Sections were incubated with primary antibodies diluted in blocking buffer at 4 °C overnight. On the second day, sections were washed with PBS and then incubated with secondary antibodies diluted in blocking buffer at room temperature for 1 h. Sections were stained with DAPI diluted in PBS and then washed with PBS and mounted with fluoro-gel mounting medium (Electron Microscopy Sciences, 1798510).

For C2C12 staining, cells were fixed in formalin at room temperature for 5 min and then blocked with blocking buffer at room temperature for 1 h. Cells were incubated with primary antibodies diluted in blocking buffer at 4 °C overnight. On the second day, cells were washed with PBS and then incubated with secondary antibodies diluted in blocking buffer at room temperature for 1 h. Cells were stained with DAPI, diluted in PBS and then washed with PBS and mounted with fluoro-gel mounting medium.

Single-myofiber isolation was performed based on a published protocol[65]. Briefly, extensor digitorum longus or soleus muscles were digested with 2 ml Collagenase I solution (2 mg ml^{-1} Collagenase type I (Worthington, #CLS-1) in F-10 medium) for 1 h at 37 °C and then triturated by hand with a wide-bore pipette to release single fibers. Fibers were fixed with formalin for 10 min at room temperature, followed by blocking buffer (PBS, 10% goat serum and 0.25% Triton X-100) for 1 h at room temperature and primary antibody (diluted in blocking buffer) overnight at 4 °C. On the second day, fibers were washed with PBS, incubated with secondary antibodies (diluted in blocking buffer) for 1 h at room temperature and mounted with fluoro-gel mounting medium on glass slides.

Muscle sections, single myofibers and C2C12 cells were imaged using a Zeiss LSM780 inverted confocal microscope and analyzed using ImageJ software. For single-myofiber analysis, longitudinal mito-Dendra2 profiles were calculated in ImageJ and aligned in MATLAB (MathWorks). The following antibodies were

used: Pax7 (AB528428, 2 µg ml^{-1}), MYH3 (BF-45, 2 µg ml^{-1}), Myogenin (F5D, 2 µg ml^{-1}), MYH (MF20, 2 µg ml^{-1}) (all from Developmental Studies Hybridoma Bank), MyoD (Santa Cruz Biotechnology, sc-377460, 1:500), laminin (Sigma-Aldrich, L9393, 1:500), Ki67 (Abcam, ab15580, 1:500), Tomm20 (Proteintech, 11802-1-AP; 1:500), myosin heavy chain type I (Sigma-Aldrich, M8421; 1:500), myosin heavy chain type II (Sigma-Aldrich, M4276, 1:500), cleaved caspase-3 (Cell Signaling Technology, 9664, 1:500), HA (Abcam, ab9110; 1:500), Alexa Fluor 594 goat anti-mouse IgG2b (A21145, 1:500), Alexa Fluor 594 goat anti-mouse IgG1 (A21125, 1:500), Alexa Fluor 488 goat anti-rabbit IgG(H+L) (A11034, 1:500), Alexa Fluor 594 goat anti-rabbit IgG(H+L) (A11012, 1:500) and Alexa Fluor 647 goat anti-mouse IgG2b (A21242, 1:500) (all from Invitrogen). TUNEL staining was performed using the Click-iT Plus TUNEL Assay kit (Invitrogen, C10618).

Retrovirus generation and infection. Mouse Scin cDNA (obtained from transOMIC technologies) or Cox4-DsRed (Addgene, 23215) were cloned into the retroviral vector pQCXIP (Clontech, 631516), and 3 µg pQCXIP-empty vector or pQCXIP-Scin-HA or pQCXIP-Cox4-DsRed plasmids with 1 µg pCL-Eco (Addgene, 12371) plasmids were transfected using PEI (Polysciences, 24765-1) into HEK293T (ATCC, CRL-11268) at 80% confluence in a six-well plate; 48 h after transfection, viral medium was collected and filtered through a 0.45-µm filter.

For C2C12 myoblasts, cells were plated the day before infection at 30% confluence and infected with viral mixture containing polybrene (Sigma-Aldrich, H9268, 6 µg ml^{-1}) for 24 h. Infected cells were selected with 2 µg ml^{-1} puromycin. After C2C12 cell line infection with Cox4-DsRed, DsRed-positive cells were sorted using FACS Aria flow cytometer (BD Biosciences).

For primary MuSCs infection, 10,000 freshly isolated MuSCs were plated in 96-well plate with growth medium (Ham's F-10 (HyClone, SH30025.01) with 10% horse serum, 1% penicillin/streptomycin and 2.5 ng ml^{-1} basic fibroblast growth factor (Peprotech, 100-18B)) overnight. MuSCs were overlaid with viral supernatant for 24 h and then transferred to wells containing 4-day C2C12 myotubes (see in vitro fusion assay below).

In vitro MuSC fusion assay. For the MuSC–myotube fusion assay, DsRed-positive C2C12 myoblasts were first cultured in growth medium (DMEM with 10% FBS and 1% penicillin/streptomycin) in an eight-well chamber slide (Thermo Fisher Scientific, 177445). When the confluence reached 90%, the culture medium was replaced with differentiation medium (DMEM with 2% horse serum and 1% penicillin/streptomycin) for 4 days to induce myotube formation. Then, 10,000 Dendra-positive MuSCs (isolated at $t = 5$ days after the first dose of tamoxifen) were then overlaid on myotube-containing wells. After incubation for an additional 4 days, cells were fixed and stained for myosin and DAPI, and the myotube fusion index was calculated as the fraction of myotube (myosin-positive) nuclei that also contained Dendra2 signal.

For the in vitro differentiation (MuSC-MuSC fusion) assay, 100,000 freshly isolated MuSCs were plated in an eight-well chamber slide (Thermo Fisher Scientific, 177445) with growth medium (Ham's F-10 (HyClone, SH30025.01) with 10% horse serum, 1% penicillin/streptomycin and 2.5 ng ml^{-1} basic fibroblast growth factor (Preprotech, 100-18B) for 24 h. The media was then switched to differentiation medium (DMEM with 2% horse serum and 1% penicillin/streptomycin) for 4 days. Cells were fixed and stained for myosin and DAPI, and the fusion index was calculated as the fraction of total nuclei in myosin-positive myotubes, based on published methods[26].

Statistical analysis. All data are represented as median and interquartile range box plots; whiskers are plotted using the Tukey method. All data are from biological replicates. No statistical tests were used to predetermine sample size. Data sets for each group of measurement were tested for normality using the Shapiro–Wilk test. If the data were not normally distributed, the data were log-transformed and retested for normality. For normally distributed data, groups were compared using the two-tailed Student's *t* test (for two groups) or one- or two-way ANOVA (for more than two groups), followed by Sidak's, Tukey's or Dunnett's test for multiple comparisons. For data that were not normally distributed, we used nonparametric testing (Mann–Whitney or Kolmogorov–Smirnov tests for two groups and Kruskal–Wallis test for multiple groups), followed by Dunn's multiple comparisons adjustment. For analyzing observed frequencies of protein-coding indels and nonsynonymous substitutions and fiber-type–specific analysis, a chi-squared test was used. Multiple independent experiments with biological replicates were performed for all reported data, and the number of biological replicates is indicated in the figures.

Reporting Summary. Further information on research design is available in the Nature Research Reporting Summary linked to this article.

Data availability

RNA-seq and mtDNA sequencing data have been deposited in the NCBI GEO (accession numbers GSE180953 and GSE180867). mtDNA sequencing mapping used GRCm38 (*M. musculus* genome; https://www.ncbi.nlm.nih.gov/assembly/GCF_000001635.20). Other data are provided within the article, source data and supplementary materials or available upon reasonable request.

Code availability

The custom code used for analysis of mtDNA sequencing is available at https://git.biohpc.swmed.edu/CRI/mtDNASeq. The RNA-seq analysis workflow is available at https://git.biohpc.swmed.edu/BICF/Astrocyte/rnaseq.git.

Received: 3 May 2021; Accepted: 8 December 2021;
Published online: 27 January 2022

References

1. Ng, Y. S. & Turnbull, D. M. Mitochondrial disease: genetics and management. *J. Neurol.* **263**, 179–191 (2016).
2. Murphy, E. et al. Mitochondrial function, biology, and role in disease: a scientific statement from the American Heart Association. *Circ. Res.* **118**, 1960–1991 (2016).
3. Granatiero, V. & Manfredi, G. Mitochondrial transport and turnover in the pathogenesis of amyotrophic lateral sclerosis. *Biology (Basel)* **8**, 36 (2019).
4. Chen, C. et al. Mitochondrial dysfunction in Parkinson's disease: cause or consequence? *Biology (Basel)* **8**, 38 (2019).
5. Liu, X. et al. Regulation of mitochondrial biogenesis in erythropoiesis by mTORC1-mediated protein translation. *Nat. Cell Biol.* **19**, 626–638 (2017).
6. Anso, E. et al. The mitochondrial respiratory chain is essential for haematopoietic stem cell function. *Nat. Cell Biol.* **19**, 614–625 (2017).
7. Ryall, J. G. et al. The NAD(+)-dependent SIRT1 deacetylase translates a metabolic switch into regulatory epigenetics in skeletal muscle stem cells. *Cell Stem Cell* **16**, 171–183 (2015).
8. Yucel, N. et al. Glucose metabolism drives histone acetylation landscape transitions that dictate muscle stem cell function. *Cell Rep.* **27**, 3939–3955 (2019).
9. Lepper, C., Partridge, T. A. & Fan, C. M. An absolute requirement for Pax7-positive satellite cells in acute injury-induced skeletal muscle regeneration. *Development* **138**, 3639–3646 (2011).
10. Sambasivan, R. et al. Pax7-expressing satellite cells are indispensable for adult skeletal muscle regeneration. *Development* **138**, 3647–3656 (2011).
11. Murphy, M. M., Lawson, J. A., Mathew, S. J., Hutcheson, D. A. & Kardon, G. Satellite cells, connective tissue fibroblasts and their interactions are crucial for muscle regeneration. *Development* **138**, 3625–3637 (2011).
12. Lepper, C., Conway, S. J. & Fan, C. M. Adult satellite cells and embryonic muscle progenitors have distinct genetic requirements. *Nature* **460**, 627–631 (2009).
13. Diaz, F., Thomas, C. K., Garcia, S., Hernandez, D. & Moraes, C. T. Mice lacking COX10 in skeletal muscle recapitulate the phenotype of progressive mitochondrial myopathies associated with cytochrome c oxidase deficiency. *Hum. Mol. Genet.* **14**, 2737–2748 (2005).
14. L'honoré, A. et al. The role of Pitx2 and Pitx3 in muscle stem cells gives new insights into P38alpha MAP kinase and redox regulation of muscle regeneration. *Elife* **7**, e32991 (2018).
15. Garcia-Prat, L. et al. Autophagy maintains stemness by preventing senescence. *Nature* **529**, 37–42 (2016).
16. Li, N. et al. Mitochondrial complex I inhibitor rotenone induces apoptosis through enhancing mitochondrial reactive oxygen species production. *J. Biol. Chem.* **278**, 8516–8525 (2003).
17. Ghelli, A. et al. Leber's hereditary optic neuropathy (LHON) pathogenic mutations induce mitochondrial-dependent apoptotic death in transmitochondrial cells incubated with galactose medium. *J. Biol. Chem.* **278**, 4145–4150 (2003).
18. Diaz, F. et al. Pathophysiology and fate of hepatocytes in a mouse model of mitochondrial hepatopathies. *Gut* **57**, 232–242 (2008).
19. Mah-Som, A. Y. et al. Reliance on Cox10 and oxidative metabolism for antigen-specific NK cell expansion. *Cell Rep.* **35**, 109209 (2021).
20. Chen, D. et al. Coupled analysis of transcriptome and BCR mutations reveals role of OXPHOS in affinity maturation. *Nat. Immunol.* **22**, 904–913 (2021).
21. Saravia, J. et al. Homeostasis and transitional activation of regulatory T cells require c-Myc. *Sci. Adv.* **6**, eaaw6443 (2020).
22. Pham, A. H., McCaffery, J. M. & Chan, D. C. Mouse lines with photo-activatable mitochondria to study mitochondrial dynamics. *Genesis* **50**, 833–843 (2012).
23. Keefe, A. C. et al. Muscle stem cells contribute to myofibres in sedentary adult mice. *Nat. Commun.* **6**, 7087 (2015).
24. Pawlikowski, B., Pulliam, C., Betta, N. D., Kardon, G. & Olwin, B. B. Pervasive satellite cell contribution to uninjured adult muscle fibers. *Skelet. Muscle* **5**, 42 (2015).
25. Mishra, P., Varuzhanyan, G., Pham, A. H. & Chan, D. C. Mitochondrial dynamics is a distinguishing feature of skeletal muscle fiber types and regulates organellar compartmentalization. *Cell Metab.* **22**, 1033–1044 (2015).
26. Millay, D. P. et al. Myomaker is a membrane activator of myoblast fusion and muscle formation. *Nature* **499**, 301–305 (2013).
27. Liu, N. et al. A Twist2-dependent progenitor cell contributes to adult skeletal muscle. *Nat. Cell Biol.* **19**, 202–213 (2017).

28. de Morree, A. et al. Alternative polyadenylation of Pax3 controls muscle stem cell fate and muscle function. *Science* **366**, 734–738 (2019).
29. Der Vartanian, A. et al. PAX3 confers functional heterogeneity in skeletal muscle stem cell responses to environmental stress. *Cell Stem Cell* **24**, 958–973 (2019).
30. Murphy, M. P. How mitochondria produce reactive oxygen species. *Biochemical J.* **417**, 1–13 (2009).
31. Hamanaka, R. B. et al. Mitochondrial reactive oxygen species promote epidermal differentiation and hair follicle development. *Sci. Signal.* **6**, ra8 (2013).
32. Tormos, K. V. et al. Mitochondrial complex III ROS regulate adipocyte differentiation. *Cell Metab.* **14**, 537–544 (2011).
33. He, F. et al. Redox mechanism of reactive oxygen species in exercise. *Front. Physiol.* **7**, 486 (2016).
34. Zuo, L., Nogueira, L. & Hogan, M. C. Reactive oxygen species formation during tetanic contractions in single isolated Xenopus myofibers. *J. Appl. Physiol.* **111**, 898–904 (2011).
35. Parker, L., McGuckin, T. A. & Leicht, A. S. Influence of exercise intensity on systemic oxidative stress and antioxidant capacity. *Clin. Physiol. Funct. Imaging* **34**, 377–383 (2014).
36. Dillard, C. J., Litov, R. E., Savin, W. M., Dumelin, E. E. & Tappel, A. L. Effects of exercise, vitamin E, and ozone on pulmonary function and lipid peroxidation. *J. Appl. Physiol. Respir. Environ. Exerc. Physiol.* **45**, 927–932 (1978).
37. Powers, S. K., Nelson, W. B. & Hudson, M. B. Exercise-induced oxidative stress in humans: cause and consequences. *Free Radic. Biol. Med.* **51**, 942–950 (2011).
38. Sens, K. L. et al. An invasive podosome-like structure promotes fusion pore formation during myoblast fusion. *J. Cell Biol.* **191**, 1013–1027 (2010).
39. Shilagardi, K. et al. Actin-propelled invasive membrane protrusions promote fusogenic protein engagement during cell-cell fusion. *Science* **340**, 359–363 (2013).
40. Hartwig, J. H. & Kwiatkowski, D. J. Actin-binding proteins. *Curr. Opin. Cell Biol.* **3**, 87–97 (1991).
41. Jiang, H. et al. Adseverin plays a role in osteoclast differentiation and periodontal disease-mediated bone loss. *FASEB J.* **29**, 2281–2291 (2015).
42. Millay, D. P., Sutherland, L. B., Bassel-Duby, R. & Olson, E. N. Myomaker is essential for muscle regeneration. *Genes Dev.* **28**, 1641–1646 (2014).
43. Zhang, H. et al. NAD(+) repletion improves mitochondrial and stem cell function and enhances life span in mice. *Science* **352**, 1436–1443 (2016).
44. Wei, W. et al. Germline selection shapes human mitochondrial DNA diversity. *Science* **364**, eaau6520 (2019).
45. Ju, Y. S. et al. Origins and functional consequences of somatic mitochondrial DNA mutations in human cancer. *Elife* **3**, e02935 (2014).
46. White, R. B., Bierinx, A. S., Gnocchi, V. F. & Zammit, P. S. Dynamics of muscle fibre growth during postnatal mouse development. *BMC Dev. Biol.* **10**, 21 (2010).
47. Bouviere, J. et al. Exercise-stimulated ROS sensitive signaling pathways in skeletal muscle. *Antioxidants* **10**, 537 (2021).
48. Morrison, D. et al. Vitamin C and E supplementation prevents some of the cellular adaptations to endurance-training in humans. *Free Radic. Biol. Med.* **89**, 852–862 (2015).
49. Bjornsen, T. et al. Vitamin C and E supplementation blunts increases in total lean body mass in elderly men after strength training. *Scand. J. Med. Sci. Sports* **26**, 755–763 (2016).
50. Ristow, M. et al. Antioxidants prevent health-promoting effects of physical exercise in humans. *Proc. Natl Acad. Sci. USA* **106**, 8665–8670 (2009).
51. Clifford, T., Jeffries, O., Stevenson, E. J. & Davies, K. A. B. The effects of vitamin C and E on exercise-induced physiological adaptations: a systematic review and Meta-analysis of randomized controlled trials. *Crit. Rev. Food Sci. Nutr.* **60**, 3669–3679 (2020).
52. Gomez-Cabrera, M. C. et al. Oral administration of vitamin C decreases muscle mitochondrial biogenesis and hampers training-induced adaptations in endurance performance. *Am. J. Clin. Nutr.* **87**, 142–149 (2008).
53. Paulsen, G. et al. Vitamin C and E supplementation hampers cellular adaptation to endurance training in humans: a double-blind, randomised, controlled trial. *J. Physiol.* **592**, 1887–1901 (2014).
54. Rossi, D. J. et al. Deficiencies in DNA damage repair limit the function of haematopoietic stem cells with age. *Nature* **447**, 725–729 (2007).
55. Nijnik, A. et al. DNA repair is limiting for haematopoietic stem cells during ageing. *Nature* **447**, 686–690 (2007).
56. Katajisto, P. et al. Stem cells. Asymmetric apportioning of aged mitochondria between daughter cells is required for stemness. *Science* **348**, 340–343 (2015).
57. Weinberg, S. E. et al. Mitochondrial complex III is essential for suppressive function of regulatory T cells. *Nature* **565**, 495–499 (2019).
58. Miura, H., Quadros, R. M., Gurumurthy, C. B. & Ohtsuka, M. Easi-CRISPR for creating knock-in and conditional knockout mouse models using long ssDNA donors. *Nat. Protoc.* **13**, 195–215 (2018).
59. Liu, L., Cheung, T. H., Charville, G. W. & Rando, T. A. Isolation of skeletal muscle stem cells by fluorescence-activated cell sorting. *Nat. Protoc.* **10**, 1612–1624 (2015).
60. Marquis, J. et al. MitoRS, a method for high throughput, sensitive, and accurate detection of mitochondrial DNA heteroplasmy. *BMC Genomics* **18**, 326 (2017).
61. Wei, W., Gomez-Duran, A., Hudson, G. & Chinnery, P. F. Background sequence characteristics influence the occurrence and severity of disease-causing mtDNA mutations. *PLoS Genet.* **13**, e1007126 (2017).
62. Stewart, J. B. et al. Simultaneous DNA and RNA mapping of somatic mitochondrial mutations across diverse human cancers. *PLoS Genet.* **11**, e1005333 (2015).
63. Livak, K. J. & Schmittgen, T. D. Analysis of relative gene expression data using real-time quantitative PCR and the 2(-Delta Delta C(T)) method. *Methods* **25**, 402–408 (2001).
64. Jing, D. et al. Tissue clearing of both hard and soft tissue organs with the PEGASOS method. *Cell Res.* **28**, 803–818 (2018).
65. Brun, C. E., Wang, Y. X. & Rudnicki, M. A. Single EDL myofiber isolation for analyses of quiescent and activated muscle stem cells. *Methods Mol. Biol.* **1686**, 149–159 (2018).

Acknowledgements

We thank the Moody Foundation Flow Cytometry Facility for assistance with FACS experiments, the Children's Research Institute Next Generation Sequencing Facility for assistance with RNA-seq experiments, the Children's Research Institute Mouse Genome Engineering Core, the UTSouthwestern Live Cell Imaging Facility, the BioHPC supercomputing facility and E. Olson for providing *Mymk*$^{f/f}$ mice. We thank R. Bassel-Duby, R. DeBerardinis, S. Morrison, E. Olson, H. Zhu and members of the Mishra laboratory for helpful discussions and suggestions during this project. This work was supported by funding from the United Mitochondrial Disease Foundation (research grant to P.M.), the National Institutes of Health (grant 1DP2ES030449-01 from the National Institute of Environmental Health Sciences, grant 1R01AR073217-01 from the National Institute of Arthritis and Musculoskeletal and Skin Diseases to P.M., grant T32-GM007062 to A.F. and grant 1F31-DK122676 from the National Institute of Diabetes and Digestive and Kidney Diseases to N.P.L.), the Moody Medical Research Institute (research grant to P.M.), the Cancer Prevention & Research Institute of Texas (scholar award RR140084 to D.G.M), the Damon Runyon Cancer Research Foundation (clinical investigator award 102-19 to D.G.M.), the National Science Foundation (Graduate Research Fellowships Program award 2019281210 to S.D.S.) and UT Southwestern Medical Center (Disease-Oriented Clinical Scholars award to D.G.M.). The funders had no role in study design, data collection and analysis, decision to publish or preparation of the manuscript.

Author contributions

X.W. and P.M. conceived the project. X.W. performed experiments, with technical assistance from S.D.S, B.B., Z.G., N.P.L. and S.S.K.V. mtDNA sequence analysis and pipeline development were performed by S.D.S. and Z.Z. *Ndufa9* conditional knockout mice were created and characterized by A.R.F. and D.G.M. Clearing experiments and imaging were performed with assistance from Y.Y and H.Z. *Qpc* and *Tfam* conditional knockout mice were generated by N.S.C. *Scinderin* conditional knockout mice were generated by M.G. X.W., S.D.S and P.M. prepared the figures and manuscript.

Competing interests

The authors declare no competing interests.

Additional information

Extended data is available for this paper at https://doi.org/10.1038/s43587-021-00164-x.

Supplementary information The online version contains supplementary material available at https://doi.org/10.1038/s43587-021-00164-x.

Correspondence and requests for materials should be addressed to Prashant Mishra.

Peer review information *Nature Aging* thanks Enrique Jaimovich and the other, anonymous, reviewer(s) for their contribution to the peer review of this work.

Reprints and permissions information is available at www.nature.com/reprints.

Publisher's note Springer Nature remains neutral with regard to jurisdictional claims in published maps and institutional affiliations.

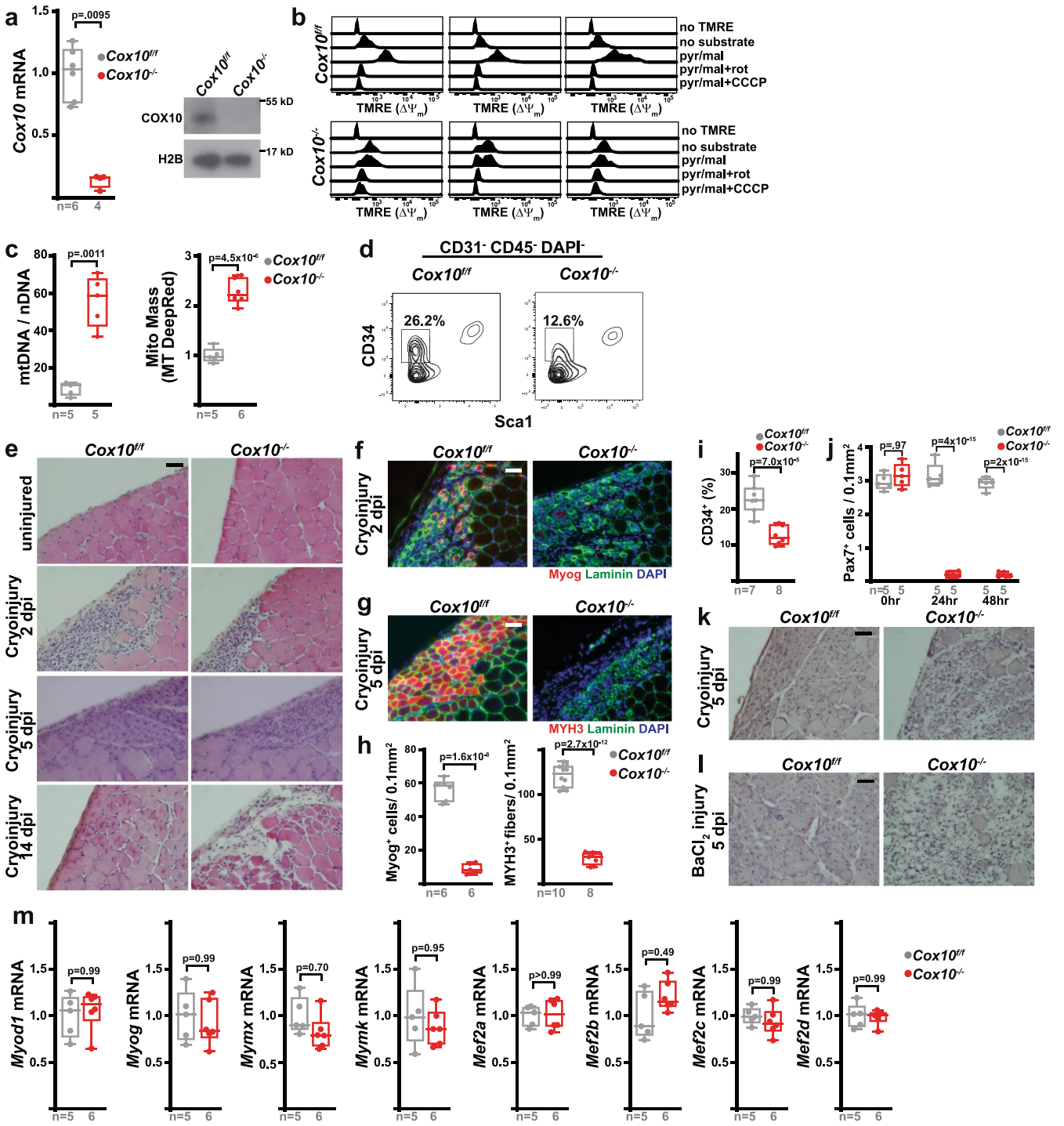

Extended Data Fig. 1 | *Cox10* deletion in MuSCs results in defective muscle regeneration. a, *Cox10* transcript and protein in MuSCs 5 days post 1st dose of tamoxifen. H2B: Histone2B. **b**, MuSC TMRE profiles in the indicated buffers. Each column represents MuSCs from an individual animal. pyr/mal, pyruvate/malate. rot, rotenone. **c**, Mitochondrial genome content (mtDNA/nDNA) and mass (Mitotracker (MT) DeepRed) in MuSCs at 5 days post 1st dose of tamoxifen. nDNA: nuclear DNA. **d**, Representative MuSC FACS profiles at 5 days post 1st tamoxifen dose. The $CD34^+$ frequency is reported as a percentage of $CD31^-CD45^-DAPI^-$ cells. **e**, Histology (H&E) of TA muscle cross-sections subject to cryoinjury. dpi, days post injury. **f**, Immunofluorescence of Myog (red), Laminin (green), and DAPI (blue) from TA muscle cross-sections 2 days post-cryoinjury. **g**, Immunofluorescence of MYH3 (red), laminin (green), and DAPI (blue) from TA muscle cross-sections 5 days post-cryoinjury. **h**, Quantitation of $Myog^+$ cells (2 days post cryoinjury) and $MYH3^+$ fibers (5 days post cryoinjury), normalized to muscle area. **i**, $CD34^+$ MuSC (as a percentage of $CD31^-CD45^-DAPI^-$ cells assessed at 5 days post 1st tamoxifen dose. **j**, $Pax7^+$ MuSC numbers (normalized to muscle area) from TA muscle cross-sections at time points after a single tamoxifen dose. p-values reflect comparisons with 0 hr data for each genotype. **k**, Histology (H&E) of TA muscle cross-sections at 5 days post cryo-injury. **l**, Histology (H&E) of TA muscle cross-sections at 5 days post-$BaCl_2$ injury. **m**, mRNA transcripts at 5 days post 1st tamoxifen dose. Statistical significance was assessed using two-tailed Mann–Whitney (a), two-tailed t-test (c,h,i), or two-way ANOVA (j,m) tests, with adjustments for multiple comparisons. Box plots indicate median values and interquartile ranges; whiskers are plotted using the Tukey method. The number of biological replicates per group is indicated. All scale bars are 50 μm. Experiments were repeated 3x (panel e), 6x (panel f), 8–10x (panel g), and 3x (panels k,l); all with similar results.

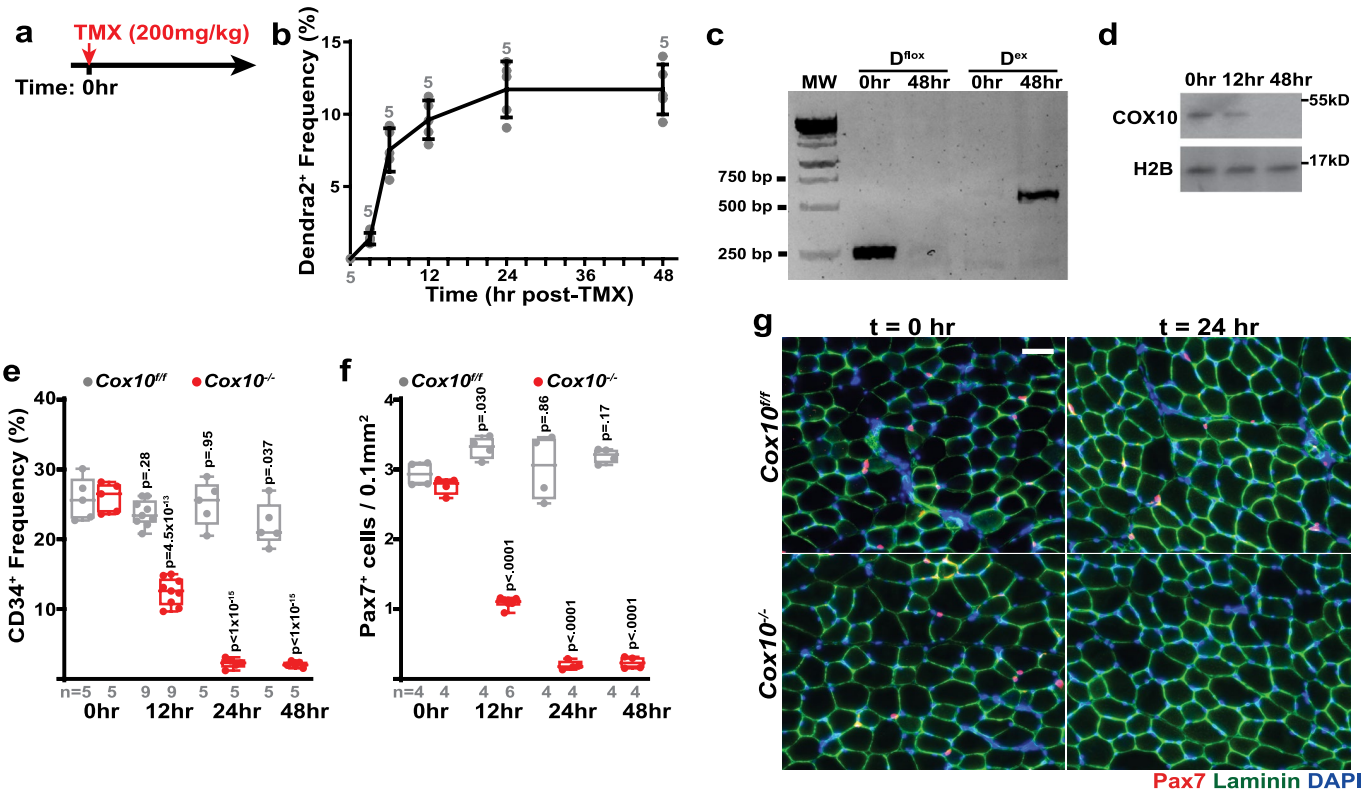

Extended Data Fig. 2 | *Cox10*$^{-/-}$ MuSCs rapidly deplete following a single dose of tamoxifen. a, Schematic of tamoxifen administration protocol used in this figure: A single, high-dose tamoxifen (TMX) administration to induce recombination and Cox10 deletion. **b**, Quantitation of Dendra2^{+} mononuclear cells at the indicated time points post-tamoxifen administration, in wild-type reporter mice (*Pax7-Cre*$^{ERT2(KARDON)}$*; D*$^{f/f}$*;*). Mean and standard deviation (error bars) are indicated. **c**, PCR-based genotyping of unrecombined mito-Dendra2 allele (D^{flox}; expected size 265 bp) and recombined mito-Dendra2 allele (D^{ex}; expected size 645 bp) in isolated MuSCs at the indicated time points post-tamoxifen administration. **d**, Cox10 levels in isolated MuSCs from *Cox10*$^{-/-}$ mice, at the indicated time points post tamoxifen administration. Histone 2B (H2B) are shown as a loading control. **e**, MuSC frequency at indicated time points post-tamoxifen administration in mice with *Cox10*$^{f/f}$ or *Cox10*$^{-/-}$ MuSCs. p-values reflect comparisons with t = 0 hr data for each genotype. **f**, Pax7^{+} cell numbers (normalized to muscle area) at different times post-tamoxifen administration. p-values reflect comparisons with t = 0 hr data for each genotype. **g**, Representative images of endogenous Pax7^{+} cells (red), laminin (green) and DAPI (blue) from tibialis anterior (TA) cross-sections of indicated mice at indicated time points post-tamoxifen administration. Scale bar, 50 μm. Statistical significance was assessed using two-way ANOVA (e,f) tests, with adjustments for multiple comparisons. Box plots indicate median values and interquartile ranges; whiskers are plotted using the Tukey method. The number of biological replicates per group is indicated in the figure. Experiments were repeated 4 times for panel g, with similar results.

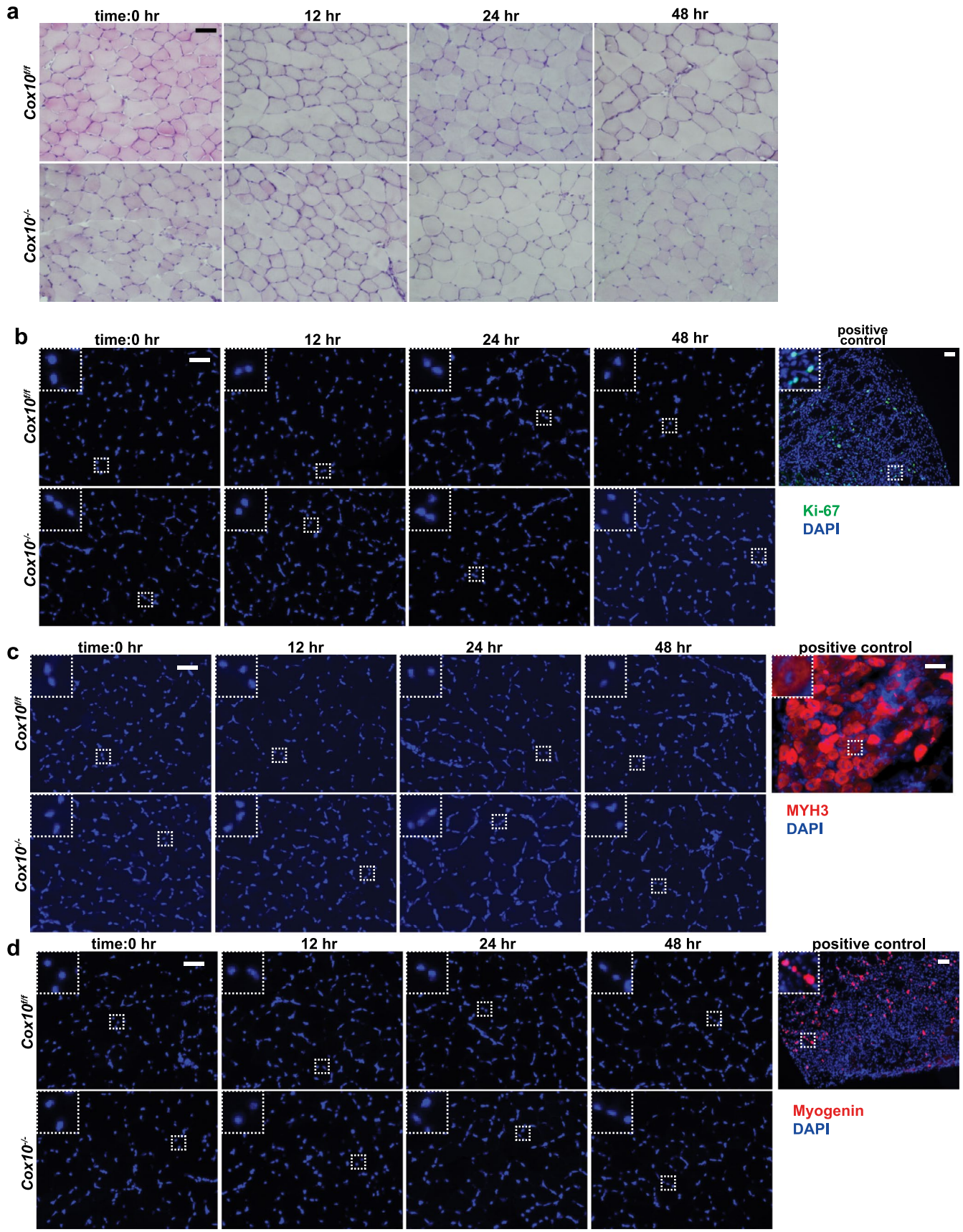

Extended Data Fig. 3 | See next page for caption.

Extended Data Fig. 3 | *Cox10*$^{-/-}$ MuSCs do not display features of activation or premature differentiation. a, Histology (H&E) of TA muscle cross-sections from animals of the indicated genotype, at different time points following a single dose of tamoxifen. **b**, Ki-67 (green) and DAPI (blue) staining of TA muscle cross-sections from animals, as described in (a). The positive control is from a wild-type animal at 2 days post cryoinjury. **c**, Same as b, but MYH3 (red) and DAPI (blue) staining. The positive control is from a wild-type animal at 5 days post cryoinjury. **d**, Same as b, but Myogenin (red) and DAPI (blue) staining. The positive control is from a wild-type animal at 2 days post cryoinjury. All scale bars are 50 μm; insets are magnified 3x. Experiments were repeated 3 times for panel a-d, with similar results.

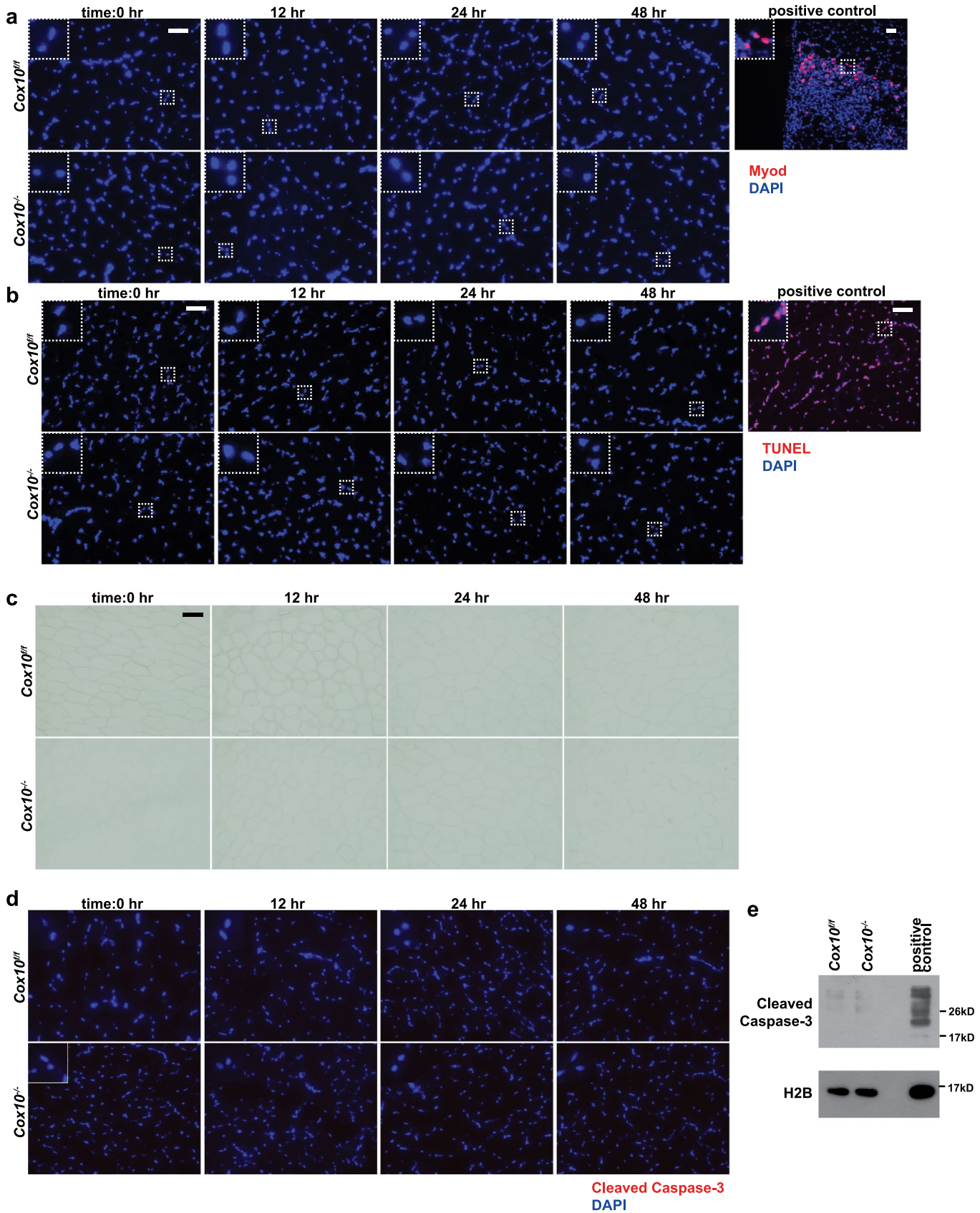

Extended Data Fig. 4 | See next page for caption.

Extended Data Fig. 4 | *Cox10*$^{-/-}$ MuSCs do not display features of senescence or apoptosis. a, Myod (red) and DAPI (blue) immunofluorescent staining of TA muscle cross-sections from animals of the indicated genotype, at different time points following a single dose of tamoxifen. The positive control is from a wild-type animal at 2 days post cryoinjury. **b**, Same as a, but TUNEL (red) and DAPI (blue) staining. For the positive control, a wild-type TA muscle cross-section was treated with DNase. **c**, Same as a, but β-galactosidase staining. **d**, Same as a, but Cleaved Caspase-3 staining (red) and DAPI (blue) staining. **e**, Cleaved Caspase-3 levels in MuSCs of the indicated genotype at 48 hr post-tamoxifen, assessed by western blot. Histone 2B (H2B) is shown as a loading control. The positive control is protein extract from *Cox10*$^{f/f}$ MuSCs treated with cytochrome c (0.25 mg/mL for 1 hr at room temperature) to induce Caspase-3 cleavage. All scale bars are 50 μm; insets are magnified 3x. Experiments were repeated 3 times for panel a-d, with similar results.

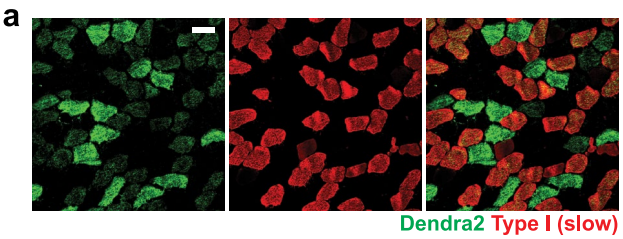

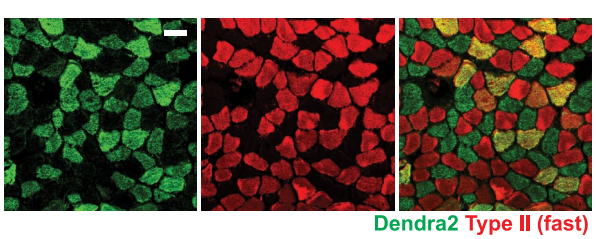

c

	Dendra2+	Dendra2-	Total
type I (slow)	701	226	927
type II (fast)	315	525	840
Total	1016	751	

$X^2 = 262.0$
$p<0.0001$

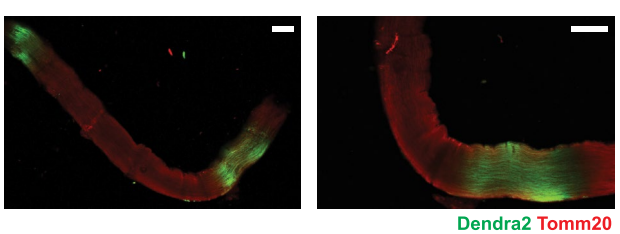

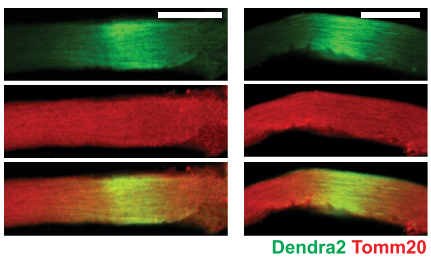

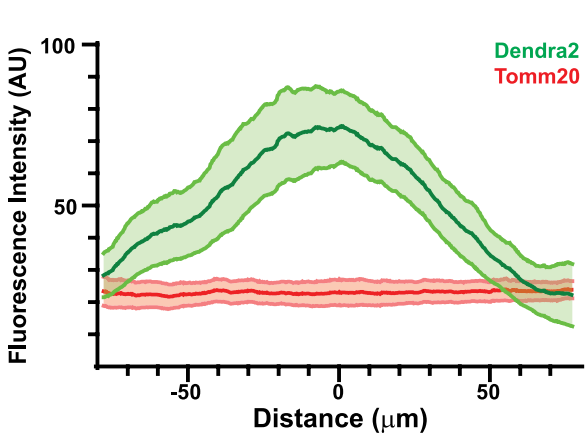

Extended Data Fig. 5 | *Cox10*$^{-/-}$ MuSCs fuse into neighboring myofibers. a, Representative immunofluorescence images from soleus muscles of *Cox10*$^{-/-}$ animals at 7 days post-the 1st dose of tamoxifen. mito-Dendra2^{+} fibers are labeled in green; type I (slow) fibers are labeled in red based on myosin heavy chain staining. Scale bar, 50 μm. **b**, Same as (a), but instead type II (fast) fibers are labeled in red based on myosin heavy chain staining. Scale bar, 50 μm. **c**, Quantitation of MuSC–myofiber fusion into type I and type II fibers from n = 4 *Cox10*$^{-/-}$ animals. Each fiber was classified based on fiber type (type I vs. type II) and Dendra2 positivity, and the number of fibers in each category are indicated. The chi-squared statistic and p-value are indicated. **d**, Representative immunofluorescent images of isolated single myofibers from *Cox10*$^{-/-}$ animals. Mito-Dendra2 domains are colored green; total mitochondrial content is imaged based on Tomm20 staining (red). Scale bar, 50 μm. **e**, Representative images of myofiber segments containing mito-Dendra2 domains (green). Tomm20 staining for mitochondrial content is shown in red. Scale bar, 50 μm. **f**, Mean fluorescent profiles and standard error envelopes for aligned mito-Dendra2 domains (green), and mitochondrial content in these regions (based on Tomm20 staining, red), for n = 15 fibers. AU, arbitrary units. Experiments were repeated 4 times for panel a,b, and 15 times for panels d,e; with similar results.

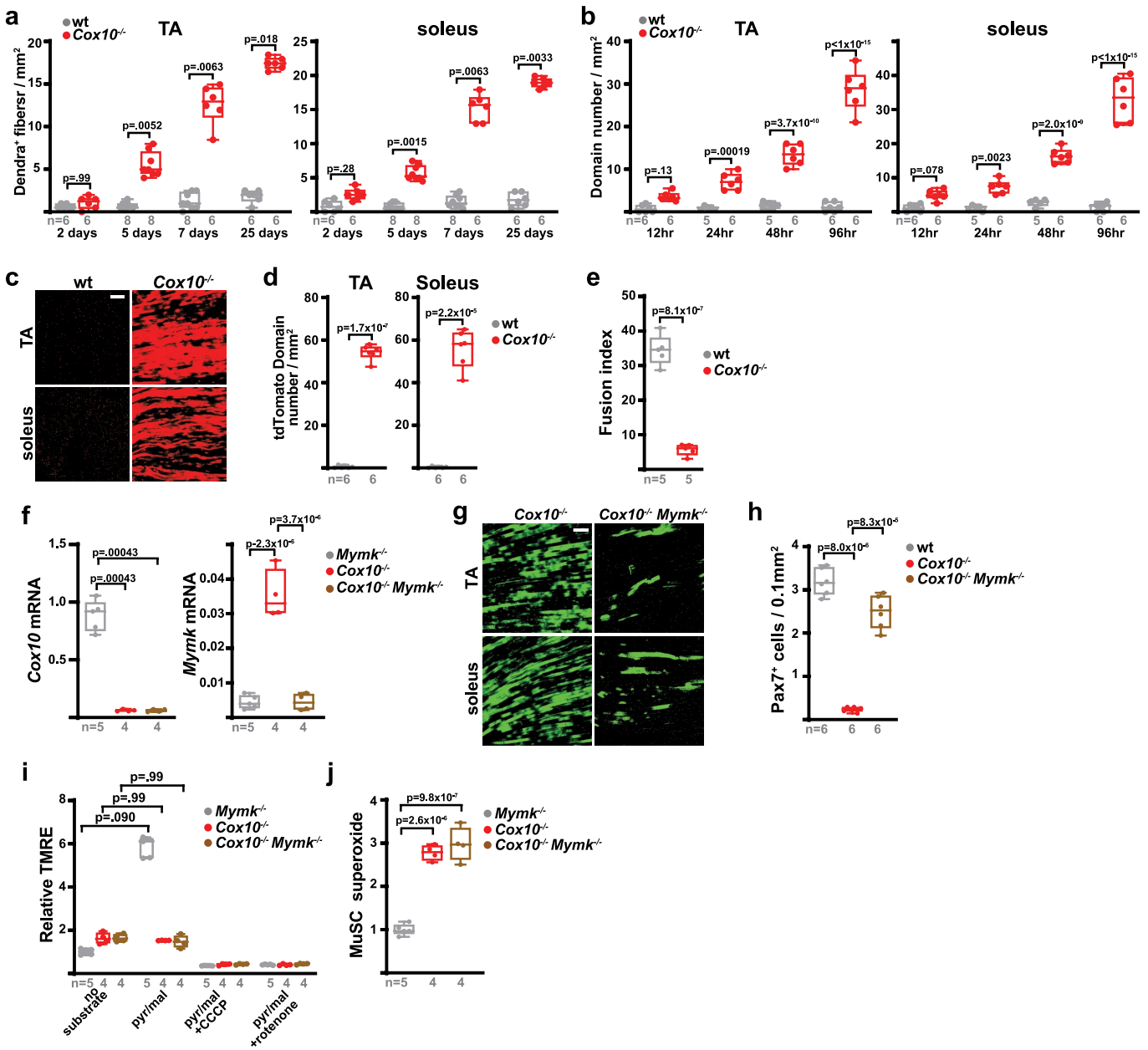

Extended Data Fig. 6 | Myomaker is required for MuSC–myofiber fusion. a, Dendra2$^+$ fiber numbers (normalized to muscle area) in TA and soleus muscles of the indicated genotypes at different times post the 1st dose of tamoxifen. **b**, mito-Dendra2+ domain number (normalized to muscle area) in TA and soleus muscles of the indicated genotype at different times post a single-high dose of tamoxifen, based on protocol in EDF 2a. **c**, Longitudinal imaging of tdTomato signal in TA and soleus muscles of the indicated genotype at 21 days post the 1st dose of tamoxifen administration. Scale bar, 200 µm. **d**, tdTomato domain number (normalized to muscle area) in myofibers of TA and soleus muscles at 21 days post the 1st dose of tamoxifen. **e**, Fusion indices in wt and *Cox10*$^{-/-}$ MuSCs subjected to *in vitro* differentiation. **f**, *Cox10* and *Myomaker* (*Mymk*) transcript levels (normalized to β2-microglobulin) in isolated MuSCs of the indicated genotype at 5 days after the 1st dose of tamoxifen. **g**, Longitudinal images of mito-Dendra2 signal in TA and soleus muscles of mice of the indicated genotype, 21 days after the 1st dose of tamoxifen. Scale bar, 200 µm. **h**, Pax7$^+$ cell numbers (normalized to muscle area) in TA muscle cross-sections of mice of the indicated genotype at 21 days after the 1st dose of tamoxifen. **i**, Relative mean TMRE fluorescence in isolated MuSCs of the indicated genotype, incubated with the indicated substrates and inhibitors. pyr/mal, pyruvate/malate. **j**, Relative mean superoxide levels in isolated MuSCs of the indicated genotype. Statistical significance was assessed using two-way ANOVA (b), Kruskal–Wallis (a,i), two-tailed t-test (d,e), or one-way ANOVA (f,h,j) tests, with adjustments for multiple comparisons. Box plots indicate median values and interquartile ranges; whiskers are plotted using the Tukey method. The number of biological replicates per group is indicated in the figure. Experiments were repeated 6 times for panels c,g, with similar results.

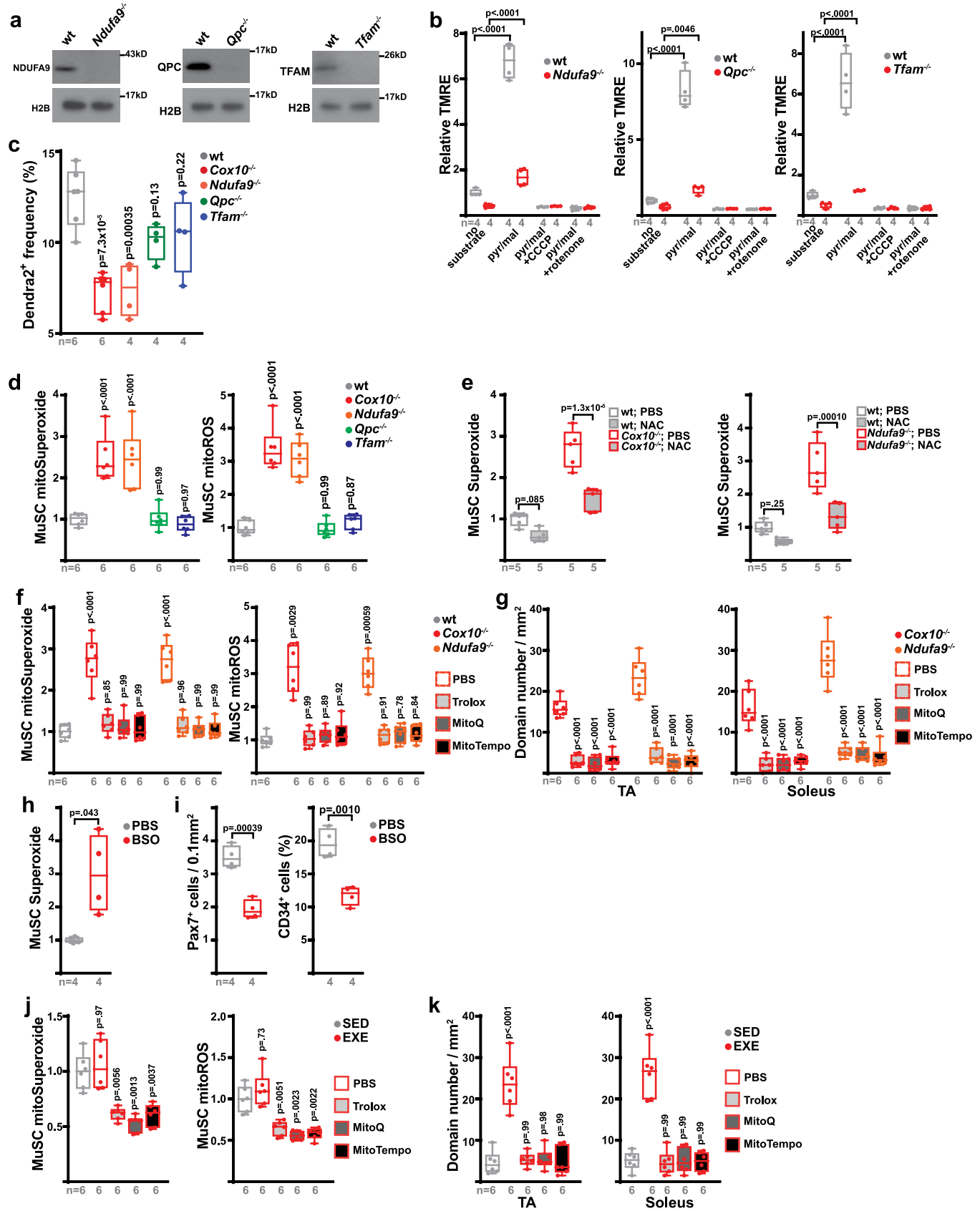

Extended Data Fig. 7 | See next page for caption.

Extended Data Fig. 7 | ROS regulate MuSC–myofiber fusion. a, Ndufa9, Qpc and Tfam levels in MuSCs at 5 days post 1st tamoxifen dose. H2B: Histone2B. **b**, Mean MuSC TMRE levels in the indicated buffers. pyr/mal, pyruvate/malate. **c**, MuSC frequency (mito-Dendra2$^+$ cells as a percentage of DAPI$^-$ mononuclear cells) at 5 days post 1st tamoxifen dose. p-values reflect comparisons with wt. **d**, Mean MuSC mitochondrial superoxide and mitochondrial total ROS (mitoROS) levels at 5 days post 1st tamoxifen dose. p-values reflect comparisons with wt. **e**, Mean MuSC superoxide levels from mice treated with vehicle (PBS) or N-acetylcysteine (NAC) at 5 days post 1st tamoxifen dose. **f**, Mean MuSC mitochondrial superoxide and mitoROS levels at 5 days post 1st tamoxifen dose, from mice treated with PBS or the indicated antioxidant. p-values reflect comparisons with wt. **g**, mito-Dendra2 domain numbers (normalized to muscle area) in muscle at 5 days post 1st tamoxifen dose from mice treated with the indicated antioxidants (or PBS). p-values reflect comparisons with 'PBS'. **h**, Mean MuSC superoxide levels from wild-type mice treated with vehicle (PBS) or BSO for 21 days. **i**, MuSC frequency (Pax7$^+$ cell number or CD34$^+$ frequency) in wild-type mice treated with vehicle (PBS) or BSO for 21 days. **j**, Mean MuSC mitochondrial superoxide and mito ROS levels from sedentary (SED) or exercised (EXE) wild-type animals treated with PBS or the indicated antioxidant. p-values reflect comparisons with 'SED'. **k**, mito-Dendra2 domain numbers (normalized to muscle area) in muscle of sedentary (SED) or exercised (EXE) mice treated with the indicated antioxidants (or PBS). p-values reflect comparisons with 'SED'. Statistical significance was assessed using one-way ANOVA (c,d,f,j,k), two-way ANOVA (b,e,g), or two-tailed t-tests (h,i), with adjustments for multiple comparisons. Box plots indicate median values and interquartile ranges; whiskers are plotted using the Tukey method. The number of biological replicates per group is indicated in the figure.

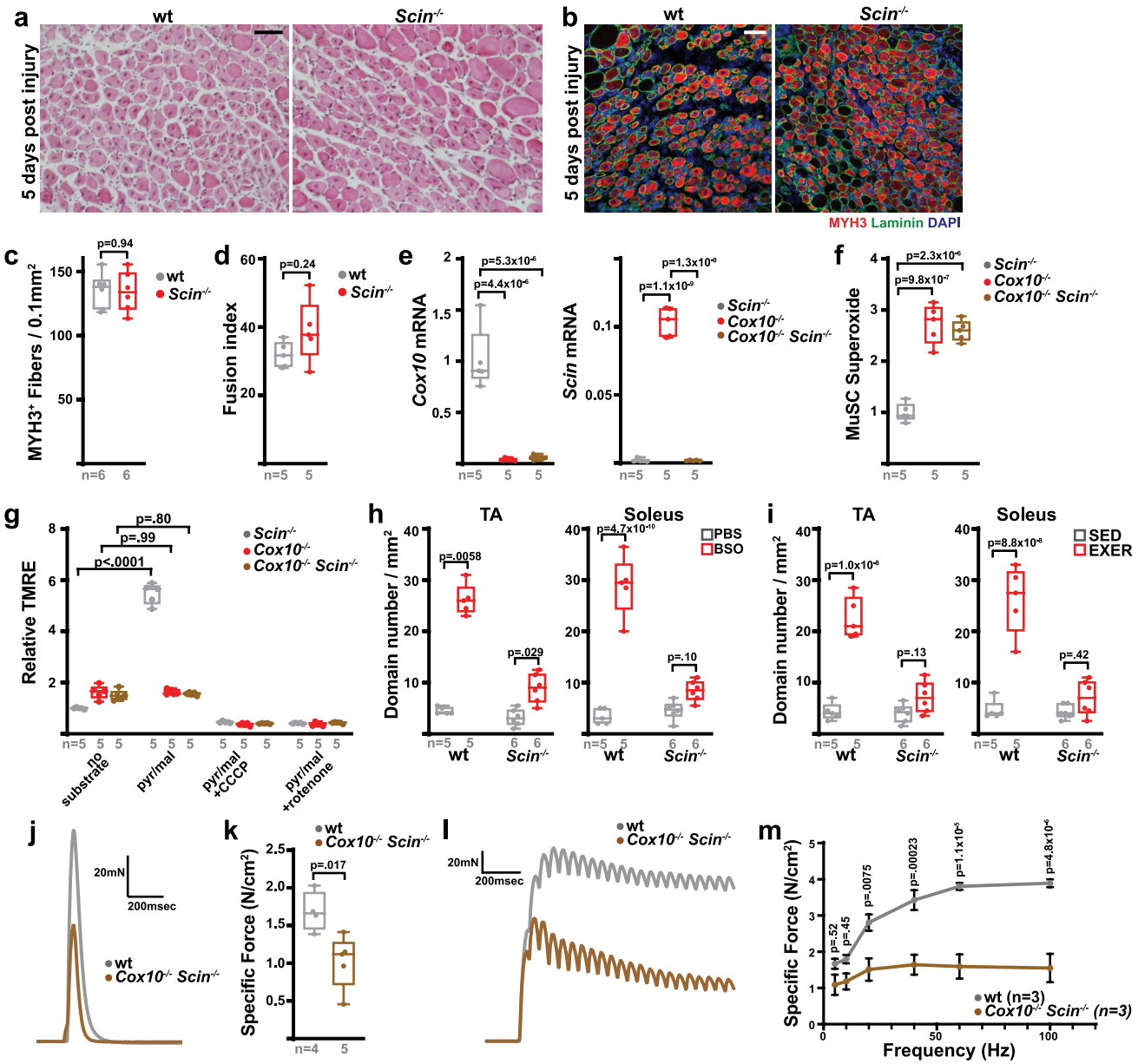

Extended Data Fig. 8 | *Scinderin* is required for MuSC–myofiber fusion. a, Histology (H&E) from TA cross-sections at 5 days post $BaCl_2$ injury. **b**, Immunofluorescence of TA cross-sections, 5 days post $BaCl_2$ injury, stained for MYH3 (red), Laminin (green), and DAPI (blue). **c**, MYH3$^+$ regenerative myofibers (normalized to muscle area) at 5 days post $BaCl_2$ injury. **d**, Fusion indices in MuSCs subjected to *in vitro* differentiation. **e**, *Cox10* and *Scin* transcript levels (normalized to β2-microglobulin) in MuSCs at 5 days post 1st tamoxifen dose. **f**, MuSC superoxide levels at 5 days post 1st tamoxifen dose. **g**, Mean MuSC TMRE fluorescence in the indicated conditions. pyr/mal, pyruvate/malate. **h**, mito-Dendra2 domain numbers (normalized to muscle area) in muscle of PBS or BSO-treated mice (for 21 days). **i**, mito-Dendra2 domain numbers (normalized to muscle area) in muscle of sedentary (SED) or exercised (EXE) mice. **j**, Representative traces of maximal twitch force from TA muscle at 21 days post-$BaCl_2$ injury. **k**, Specific force for maximal twitch from TA muscles at 21 days post-$BaCl_2$ injury. **l**, Representative traces of tetanic force generation from TA muscles (at 21 days post-$BaCl_2$ injury) subjected to a 20 Hz stimulus. **m**, Force-frequency relationship from TA muscles at 21 days post-$BaCl_2$ injury. Statistical significance was assessed using two-tailed t-test (c,d,k), Kruskal–Wallis (h), one-way ANOVA (e,f), or two-way ANOVA (g,h,i,m) tests, with adjustments for multiple comparisons. Box plots indicate median values and interquartile ranges; whiskers are plotted using the Tukey method. The number of biological replicates per group is indicated. All scale bars are 50 μm. Experiments were repeated 3x (panel a), 6x (panel b); all with similar results.

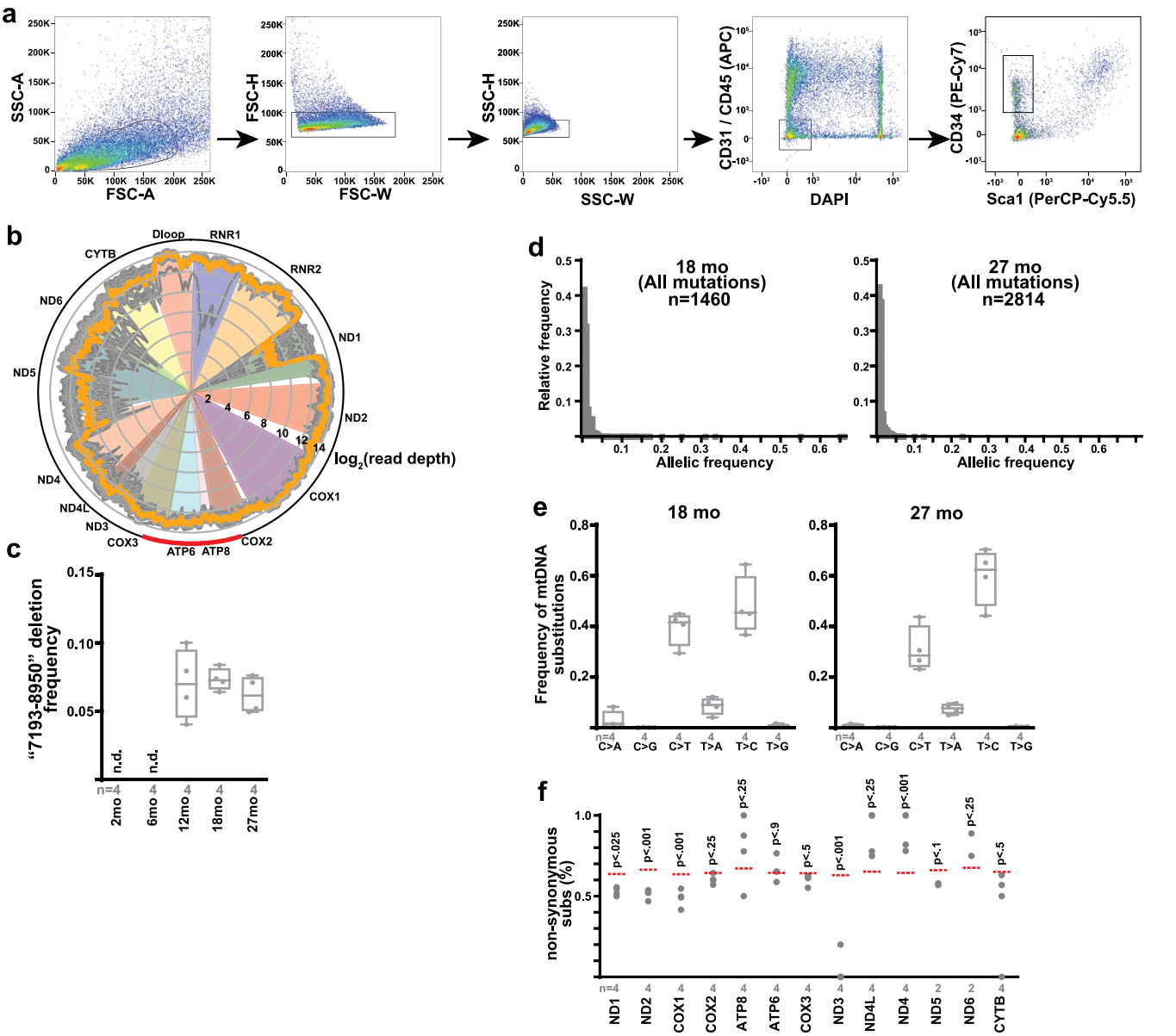

Extended Data Fig. 9 | Aging MuSCs accumulate mtDNA mutations. a, Representative images for FACS isolation of murine MuSCs. Cells were first gated by forward scatter (FSC) and side scatter (SSC) to remove doublets. MuSCs were identified by negative gating for DAPI, CD31, CD45, Sca1, and positive gating for CD34. **b**, Read depth across the mitochondrial genome for all samples (gray traces), displayed using a $\log_2$ scale. Average read depth for all samples shown in orange. The red arc indicates the position of the common "7193-8950" deletion. **c**, Deletion frequency of the "7193-8950" deletion detected in MuSCs from mice of the indicated age. n.d, not detected. **d**, Histogram of allelic frequencies for all detected mtDNA mutations in MuSCs from 18 month old and 27 month old mice. The number of identified mutations is indicated. **e**, Mutational signature of mtDNA substitutions in MuSCs from 18 month old and 27 month old mice. **f**, The observed frequencies of nonsynonymous substitutions in each mtDNA gene from isolated MuSCs of 27 month old mice. The expected frequency is indicated as the dashed red line. p-values are calculated from chi-squared test. Box plots indicate median values and interquartile ranges; whiskers are plotted using the Tukey method. The number of biological replicates per group is indicated in the figure.

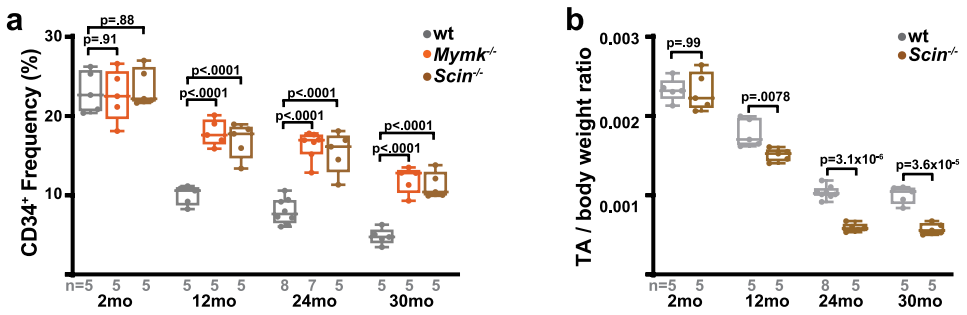

Extended Data Fig. 10 | MuSC–myofiber fusion regulates MuSC numbers during aging. a, Quantitation of MuSC frequency (CD34⁺ %) in mice of the indicated genotypes and ages. **b**, Normalized TA muscle weight at 21 days post-$BaCl_2$ injury in mice of the indicated genotypes and ages. Statistical significance was assessed using two-way ANOVA (a,b) tests, with adjustments for multiple comparisons. Box plots indicate median values and interquartile ranges; whiskers are plotted using the Tukey method. The number of biological replicates per group is indicated in the figure.

nature research

Corresponding author(s): Mishra, Prashant

Last updated by author(s): 10/29/2021

Reporting Summary

Nature Research wishes to improve the reproducibility of the work that we publish. This form provides structure for consistency and transparency in reporting. For further information on Nature Research policies, see our Editorial Policies and the Editorial Policy Checklist.

Statistics

For all statistical analyses, confirm that the following items are present in the figure legend, table legend, main text, or Methods section.

n/a	Confirmed
☐	☒ The exact sample size (*n*) for each experimental group/condition, given as a discrete number and unit of measurement
☐	☒ A statement on whether measurements were taken from distinct samples or whether the same sample was measured repeatedly
☐	☒ The statistical test(s) used AND whether they are one- or two-sided *Only common tests should be described solely by name; describe more complex techniques in the Methods section.*
☒	☐ A description of all covariates tested
☐	☒ A description of any assumptions or corrections, such as tests of normality and adjustment for multiple comparisons
☐	☒ A full description of the statistical parameters including central tendency (e.g. means) or other basic estimates (e.g. regression coefficient) AND variation (e.g. standard deviation) or associated estimates of uncertainty (e.g. confidence intervals)
☐	☒ For null hypothesis testing, the test statistic (e.g. *F*, *t*, *r*) with confidence intervals, effect sizes, degrees of freedom and *P* value noted *Give P values as exact values whenever suitable.*
☒	☐ For Bayesian analysis, information on the choice of priors and Markov chain Monte Carlo settings
☒	☐ For hierarchical and complex designs, identification of the appropriate level for tests and full reporting of outcomes
☒	☐ Estimates of effect sizes (e.g. Cohen's *d*, Pearson's *r*), indicating how they were calculated

Our web collection on statistics for biologists contains articles on many of the points above.

Software and code

Policy information about availability of computer code

Data collection	CFX 384 Real-Time System (SN027118) for qPCR and qRTPCR experiments; WAVE(v.2.4.1.1) for Seahorse experiments; WinDaq (v3.0.7) for collection of force data; Zeiss ZEN (v.14.0.0.201) for collection of imaging data; FACSDiva (v.8.0.2) for collection of flow cytometry data.
Data analysis	ImageJ (v8.0.2) for image analysis; Graphpad Prism 8 (v8.3.0) , Microsoft Excel (2013) and MatLab (R2015a) for data and statistical analysis; FlowJo (v.10.6.1) for analysis of flow cytometry data. Workflow (https://git.biohpc.swmed.edu/BICF/Astrocyte/rnaseq.git) for RNA-seq mapping and analysis. FastQC 0.11.8, TrimGalore 0.6.4, MapSplice2 2.2.1, Picard 2.23.1, SAMtools 1.9.0, and bam-readcount 0.8.0, regtools 0.5.1, bedtools 2.29.2 for mtDNA sequencing and analysis. Custom Code available at https://git.biohpc.swmed.edu/CRI/mtDNASeq

For manuscripts utilizing custom algorithms or software that are central to the research but not yet described in published literature, software must be made available to editors and reviewers. We strongly encourage code deposition in a community repository (e.g. GitHub). See the Nature Research guidelines for submitting code & software for further information.

Data

Policy information about availability of data

All manuscripts must include a data availability statement. This statement should provide the following information, where applicable:

- Accession codes, unique identifiers, or web links for publicly available datasets
- A list of figures that have associated raw data
- A description of any restrictions on data availability

RNA sequencing and mtDNA sequencing data are available at the NCBI GEO website (GSE180953, GSE180867). mtDNA sequencing mapping used GRCm38 (Mus musculus genome; https://www.ncbi.nlm.nih.gov/assembly/GCF_000001635.20). Other data are provided within the manuscript, source data and supplementary materials.

Field-specific reporting

Please select the one below that is the best fit for your research. If you are not sure, read the appropriate sections before making your selection.

☒ Life sciences ☐ Behavioural & social sciences ☐ Ecological, evolutionary & environmental sciences

For a reference copy of the document with all sections, see nature.com/documents/nr-reporting-summary-flat.pdf

Life sciences study design

All studies must disclose on these points even when the disclosure is negative.

Sample size	All sample sizes were based on standard protocols and publications in the muscle stem cell field, where anywhere from 3-10 biological replicate are analyzed per experimental group. For examples, please see PMID: 31699935, 27894125, 31534153, 26153230. No statistical test was performed to predetermine sample size.
Data exclusions	No data was excluded.
Replication	The RNA-sequencing and mtDNA sequencing experiments were performed once, using four independent biological replicates in each group. No attempts to replicate were performed, and biological replicates were similar in nature. All other experiments were performed, at least, in triplicate and reproducible across independent experiments.
Randomization	For experiments with drug or exercise treatments, recipient mice were randomly allocated between experimental groups. For all other experiments, mice were allocated solely based on genotype. All mice were housed in the same animal room under identical conditions, and analyzed at similar ages, with no other covarying variables evident. Male and female animals were used in all expereiments, and sex specific differences were not present in any experiments.
Blinding	For all experiments, investigators were not blinded as experiments were performed and analyzed by the same indiviauls, and the collected data were quantitative and objective in nature.

Reporting for specific materials, systems and methods

We require information from authors about some types of materials, experimental systems and methods used in many studies. Here, indicate whether each material, system or method listed is relevant to your study. If you are not sure if a list item applies to your research, read the appropriate section before selecting a response.

Materials & experimental systems

n/a	Involved in the study
☐	☒ Antibodies
☐	☒ Eukaryotic cell lines
☒	☐ Palaeontology and archaeology
☐	☒ Animals and other organisms
☒	☐ Human research participants
☒	☐ Clinical data
☒	☐ Dual use research of concern

Methods

n/a	Involved in the study
☒	☐ ChIP-seq
☐	☒ Flow cytometry
☒	☐ MRI-based neuroimaging

Antibodies

Antibodies used

For western blot:
Cox10 (Abcam, #ab84053,1:1000)
Qpc (Proteintech, #14975-1-AP, 1:1000)
Tfam (Santa Cruz Biotechnology, #sc-166965, 1:1000)
Scin (Santa Cruz Biotechnology, #sc-376136, 1:000)
Ndufa9 (Thermo Fisher, #459100, 1:2000)
Cleaved Caspase-3 (Cell Signaling Technology, #9664, 1:1000)
β-actin (Cell Signaling, #4970, 1:5000)
Histone H2B (Santa Cruz Biotechnology, #sc-515808, 1:1000)

For flow cytometry:
APC-conjugated anti-mouse CD31 (BioLegend, clone MEC13.3, #102510, 1:100)
APC-conjugated anti-mouse CD45 (BioLegend, clone 30-F11, #103112, 1:100)
PerCP-Cy5.5-conjugated anti-mouse Sca-1 (Invitrogen, Clone D7, #45598182, 1:100)
Biotin-conjugated anti-mouse CD34 (Invitrogen, clone RAM34, #13034181, 1:100)

For immunofluorescence staining:

Pax7 (Developmental Studies Hybridoma Bank, #AB528428, 2µg/ml)
MYH3 (Developmental Studies Hybridoma Bank, #BF-45, 2µg/ml)
Myogenin (Developmental Studies Hybridoma Bank, #F5D, 2µg/ml)
MYH (Developmental Studies Hybridoma Bank, #MF20, 2µg/ml)
MyoD (Santa Cruz Biotechnology, #sc-377460, 1:500)
Laminin (Sigma-Aldrich, #L9393, 1:500)
Ki67 (Abcam, #ab15580, 1:500)
Tomm20 (Proteintech, #11802-1-AP, 1:500)
Myosin Heavy Chain type I (Sigma, #M8421, 1:500)
Myosin Heavy Chain type II (Sigma, #M4276, 1:500)
Cleaved Caspase 3 (Cell Signaling Technology, #9664, 1:500)
HA (Abcam, #ab9110, 1:500)
Alexa Fluor 594 goat anti-mouse IgG2b (Thermo Fisher, #A21145, 1:500)
Alexa Fluor 594 goat anti-mouse IgG1 (Thermo Fisher, #A21125, 1:500)
Alexa Fluor 488 goat anti-rabbit IgG(H+L) (Thermo Fisher, #A11034, 1:500)
Alexa Fluor 594 goat anti-rabbit IgG(H+L) (Thermo Fisher, #A11012, 1:500)
Alexa Fluor 647 goat anti-mouse IgG2b (Thermo Fisher, #A21242, 1:500)

Validation

Cox10 (Abcam, #ab84053) - tested applications: western blot. Species reactivity: human, mouse. Product citations: PMID 28148912, and tested by Jackson Lab (http://tumor.informatics.jax.org/mtbwi/antibody.jsp).
Qpc (Proteintech, #14975-1-AP) - tested applications: western blot, Species reactivity: human, mouse, rat. Product citations: 6 (https://www.ptglab.com/products/UQCRQ-Antibody-14975-1-AP.htm#publications).
Tfam (Santa Cruz Biotechnology, #sc-166965) - tested applications: western blot. Species reactivity: mouse, rat, human. Product citations: 40 (https://www.scbt.com/p/mttfa-antibody-f-6).
Scin (Santa Cruz Biotechnology, #sc-376136) - tested applications: western blot. Species reactivity: mouse, rat, human. Product citations: 2 (https://www.scbt.com/p/adseverin-antibody-c-2).
Ndufa9 (Thermo Fisher, #459100) - tested applications: western blot. Species reactivity: mouse, human, rat. Product citations: 19 (https://www.thermofisher.com/antibody/product/NDUFA9-Antibody-clone-20C11B11B11-Monoclonal/459100). Verified in knockdown experiments by manufacturer.
Cleaved Caspase-3 (Cell Signaling Technology, #9664) - tested applications: western blot, immunofluorescence. Species reactivity: human, mouse, rat, monkey. Product citations: 3226 (https://www.cellsignal.com/products/primary-antibodies/cleaved-caspase-3-asp175-5a1e-rabbit-mab/9664).
β-actin (Cell Signaling, #4970) - tested applications: western blot. Species reactivity: human, mouse, rat. Product citations: 3054 (https://www.cellsignal.com/products/primary-antibodies/b-actin-13e5-rabbit-mab/4970).
Histone H2B (Santa Cruz Biotechnology, #sc-515808) - tested aplications: western blot. Species reactivity: human, mouse, rat. Product citations: 8 (https://www.scbt.com/p/histone-h2b-antibody-a-6).
APC-conjugated anti-mouse CD31 (BioLegend, clone MEC13.3, #102510) - tested applications: FACS. Species reactivity: mouse. Product citations: 40 (https://www.biolegend.com/en-us/products/purified-anti-mouse-cd31-antibody-380).
APC-conjugated anti-mouse CD45 (BioLegend, clone 30-F11, #103112) - tested applications: FACS. Species reactivity: mouse. Product citations: 136 (https://www.biolegend.com/en-us/products/apc-anti-mouse-cd45-antibody-97).
PerCP-Cy5.5-conjugated anti-mouse Sca-1 (Invitrogen, Clone D7, #45598182) - tested applications: FACS. Species reactivity: mouse. Product citations: 84 (https://www.thermofisher.com/antibody/product/Ly-6A-E-Sca-1-Antibody-clone-D7-Monoclonal/45-5981-82).
Biotin-conjugated anti-mouse CD34 (Invitrogen, clone RAM34, #13034181) - tested applications: FACS. Species reactivity: mouse. Product citations: 93 (https://www.thermofisher.com/antibody/product/CD34-Antibody-clone-RAM34-Monoclonal/13-0341-81).
Pax7 (Developmental Studies Hybridoma Bank, #AB528428) - tested applications: immunofluorescence. Species reactivity: mouse. Product citations: 112 (https://dshb.biology.uiowa.edu/PAX7).
MYH3 (Developmental Studies Hybridoma Bank, #BF-45) - tested applications: immunofluorescence. Species reactivity: mouse, rat. Product citations: 7 (https://dshb.biology.uiowa.edu/BF-45).
Myogenin (Developmental Studies Hybridoma Bank, #F5D) - tested applications: immunofluorescence. Species reactivity: mouse. Product citations: 34 (https://dshb.biology.uiowa.edu/F5D).
MYH (Developmental Studies Hybridoma Bank, #MF20) - tested applications: immunofluorescence. Species reactivity: mouse. Product citations: 166 (https://dshb.biology.uiowa.edu/MF-20).
MyoD (Santa Cruz Biotechnology, #sc-377460) - tested applications: immunofluorescence. Species reactivity: mouse. Product citations: 71 (https://www.scbt.com/p/myod-antibody-g-1).
Laminin (Sigma-Aldrich, #L9393) - tested applications: immunofluorescence. Species reactivity: mouse, human. Independent antibody verifcation by manufacturer (https://www.sigmaaldrich.com/US/en/product/sigma/l9393). Product citations: 1259.
Ki67 (Abcam, #ab15580) - tested applications: immunofluorescence. Species reactivity: mouse, human. Validated by manufacturer using knockout experiments (https://www.abcam.com/Ki67-antibody-ab15580.html). Product citations: 2829.
Tomm20 (Proteintech, #11802-1-AP) - tested applications: immunofluorescence. Species reactivity: human,mouse. Product citations: 173 (https://www.ptglab.com/products/TOM20-Antibody-11802-1-AP.htm).
Myosin Heavy Chain type I (Sigma, #M8421) - tested applications: immunofluorescence. Species reactivity: mouse. Product citations: 245 (https://www.sigmaaldrich.com/US/en/product/sigma/m8421).
Myosin Heavy Chain type II (Sigma, #M4276) - tested applications: immunofluorescence. Species reactivity: mouse. Product citations: 331 (https://www.sigmaaldrich.com/US/en/search/m4276).
Cleaved Caspase 3 (Cell Signaling Technology, #9664) - tested applications: western blot, immunofluorescence. Species reactivity: human, mouse, rat, monkey. Product citations: 3226 (https://www.cellsignal.com/products/primary-antibodies/cleaved-caspase-3-asp175-5a1e-rabbit-mab/9664).
HA (Abcam, #ab9110) - tested applications: immunofluorescence. Species reactivity: n/a. Verified by manufacturer using overexpression studies. Product citations: 899 (https://www.abcam.com/ha-tag-antibody-chip-grade-ab9110.html).

Eukaryotic cell lines

Policy information about cell lines

Cell line source(s)	Mouse C2C12 cell line, ATCC #CRL-1772 Human HEK293T, ATCC #CRL-1573
Authentication	Cell lines were authenticated via STR analysis.
Mycoplasma contamination	All cell lines were tested negative for mycoplasma contamination.
Commonly misidentified lines (See ICLAC register)	HEK293T cells are commonly confused for HeLa cells. This did not matter for this study as the cells were only used to produce viral particles.

Animals and other organisms

Policy information about studies involving animals; ARRIVE guidelines recommended for reporting animal research

Laboratory animals	Cox10f/f (strain 024697), Pax7-CreERT2(FAN) (strain 012476), Pax7-CreERT2(KARDON) (strain 017763), C57BL/6 (strain 000664), tdTomatof/f (strain 007914) and mito-Dendra2f/f (strain 018385) were purchased from The Jackson Laboratory. Qpcf/f and Tfamf/f mice were from Dr. Navdeep S. Chandel (Northwestern University Feinberg School of Medicine) Mykf/f mouse was from Dr. Eric N. Olson (University of Texas Southwestern Medical Center) Scinf/f was from Dr. Michael Glogauer (University of Toronto) The Ndufa9f/f conditional knockout mouse was generated utilizing the Easi-CRISPR workflow (see methods). Both male and female mice were used in all experiments, and sex specific differences were not evident in any experiments. Unless otherwise noted, experiments were performed for all animal strains at 6-8 weeks of age. For aging studies in figures 6 (C57Bl/6 strain), and figure 7 (mito-Dendra2f/f, mykf/f and Scinf/f strains), the age of animals are indicated in the figure and text. Animals were housed at 72degrees fahrenheit (range 68-79), 50% humidity (range 30-70%), and a 12 hr light cycle (6am-6pm). All animal protocols were approved by the University of Texas Southwestern Institutional Animal Care and Use Committee (protocol 101323), and all relevant guidelines were adhered to while carrying out this study.
Wild animals	This study did not involve wild animals.
Field-collected samples	No field-collected samples were used in the study.
Ethics oversight	All mice were housed in the Animal Resource Center at the University of Texas Southwestern Medical Center under a 12 hr light-dark cycle and were fed ad libitum. All animal protocols were approved by the University of Texas Southwestern Institutional Animal Care and Use Committee with APN-2015-101323.

Note that full information on the approval of the study protocol must also be provided in the manuscript.

Flow Cytometry

Plots

Confirm that:

☒ The axis labels state the marker and fluorochrome used (e.g. CD4-FITC).

☒ The axis scales are clearly visible. Include numbers along axes only for bottom left plot of group (a 'group' is an analysis of identical markers).

☒ All plots are contour plots with outliers or pseudocolor plots.

☒ A numerical value for number of cells or percentage (with statistics) is provided.

Methodology

Sample preparation	Following carbon dioxide asphyxiation and cervical dislocation, skeletal muscle was rapidly dissected and sequential digested with Collagenase II and Dispase at 37°C. Mononucleated cells were collected through a 70 um cell strainer, and suspended in HBSS with 2% horse serum.
Instrument	FACSAria (BD Biosciences)
Software	FACSAria (BD Biosciences)
Cell population abundance	Cell population and purity were determined by comparison with the negative control.

Gating strategy

For cell surface markers gating, mononucleated cells were first gated by forward scatter (FSC) and side scatter (SSC) to remove doublets. MuSCs were identified by negative gating for DAPI, CD31, CD45, Sca1, and positive gating for CD34.
For Dendra gating, mononucleated cells were first gated by forward scatter (FSC) and side scatter (SSC) to remove doublets. MuSCs were identified by negative gating for DAPI and positive gating for GFP.

☒ Tick this box to confirm that a figure exemplifying the gating strategy is provided in the Supplementary Information.